

JGR Earth Surface

RESEARCH ARTICLE

10.1029/2019JF005203

Key Points:

- Stability of deep-seated landslides is determined by the competition of temperature evolution of the basal material and seepage force
- The Vaiont landslide turned unstable before the last depletion of the lake, becoming unresponsive to seepage changes
- The Shuping landslide in the three Gorges valley features stable seepage when the reservoir level increases

Correspondence to:

C. Seguí, carolina.segui@duke.edu

Citation:

Seguí, C., Rattez, H., & Veveakis, M. (2020). On the stability of deep-seated landslides. The cases of Vaiont (Italy) and shuping (Three Gorges Dam, China). Journal of Geophysical Research: Earth Surface, 125, e2019JF005203. https://doi.org/10.1029/2019JF005203

Received 13 JUN 2019 Accepted 26 MAY 2020 Accepted article online 15 JUN 2020

On the Stability of Deep-Seated Landslides. The Cases of Vaiont (Italy) and Shuping (Three Gorges Dam, China)

Carolina Seguí¹, Hadrien Rattez¹, and Manolis Veveakis¹

¹Civil and Environmental Engineering Department, Duke University, Durham, NC, USA

Abstract Deep-seated landslides can have catastrophic impacts on human life and infrastructure when they suddenly fail. These events are devastating because of the large volumes of soil and rock masses involved and their often long runout. The present study suggests an energy-based method to determine when a landslide becomes unstable, giving critical values for measurable variables (velocity and basal temperature) up to which remediation actions can be deployed. This work focuses on large ancient landslides reactivated by dam-related water table variations that modify landslide stability. The main hypothesis of this work is that most of the deformation of deep-seated landslides is concentrated on a thin, basal shear band forming the sliding surface. In particular, this assumption allows an approximation of deep-seated landslides as elastic/rigid blocks sliding over a viscoplastic shear band, featuring weak phases like expansive clays. When the landslide moves, it causes friction in the shear band that raises the temperature of the clays until they become unstable and collapse catastrophically through a thermal runaway instability. The model is applied to the Vaiont landslide in Northern Italy and the Shuping landslide next to the Three Gorges Dam in China. The results of the model reproduce the sliding behavior of both landslides and provide constraints on the critical points of stability.

1. Introduction

Large, deep-seated landslide failure can be accompanied by a catastrophic impact on societies and infrastructures. This kind of landslide is often preceded by large periods (on the order of several years) of creep until they collapse suddenly without previous warning. Thus, the main question that arises from these events is: why after years of slow movement (cm/year) deep-seated landslides collapse in minutes? Some of these slides are ancient landslides that remained dormant during centuries and reactivated (due to human interaction), remaining active (from few years to tens of years) until they fail (in minutes). Because of this evolution, deep-seated landslides present a formidable challenge in their failure prediction.

Common points of focus in landslide modeling include the study of external factors that would deteriorate the stability of a slope. These factors include, for example, groundwater variations due to precipitation or dam construction and seismic activity (Terzaghi, 1950). Both of these factors can directly change the loading conditions of the landslide (through the stresses) and, therefore, the factor of safety (Song et al., 2014; Wang et al., 2017; Yu et al., 2017). However, the factor of safety is a static quantity (calculated from the stresses only) and is of restricted validity in a—predominantly kinematic—creeping landslide. This leads to the necessity of replacing the concept of factor of safety with a real-time assessment tool. Such a tool was suggested by Saito (1965, 1969), and later generalized by Voight (1988), who implied that taking the velocity data from the field and calculating the inverse velocity leads to an estimated time of the collapse of the landslide. This approach is based on extrapolating the last values of the inverse velocity until it reaches zero (i.e., displacement goes to infinity). Hence, at the time that inverse velocity is zero, the landslide accelerates catastrophically (Helmstetter et al., 2004; Sornette et al., 2004). More recently, Ma et al. (2017) and Zhao et al. (2016) generalized the inverse velocity further, by proposing forecasting models of landslide failure with probabilistic models of the displacements and regression of the groundwater data, respectively. These techniques rely on empirical observation of deep-seated landslides but provide useful insight on the phenomenology of the latest stages of large Earth slides. It seems that modeling of landslides should be enriched with internal factors of instability (Terzaghi, 1950), as physical mechanisms that can directly change the material's properties (such as strength and friction coefficient) without requiring changes in the loading stresses, and allow the slide to transition from secondary (i.e., quasi-stable) to tertiary (unstable) creep.

©2020. American Geophysical Union. All Rights Reserved.



Several studies (e.g., Kilburn & Petley, 2003) point out that the basal sliding surface (or shear band), as the weakest part of the landslide, is indeed where such internal factors of instability would be of major importance since the sliding surface is where the deformation of the landslide is concentrated. Thus, focusing on understanding the behavior of the shear band could allow us to constrain the failure mechanism of a large deep-seated landslide. It is common that deep-seated landslides present clays as the material forming their sliding surface. Clays frequently exhibit thermal softening behavior in their mechanical response (Hueckel & Baldi, 1990; Vardoulakis, 2002b, Veveakis et al., 2010). Therefore, when a landslide activates it can enter a positive thermal feedback loop (Vardoulakis, 2002b; Veveakis et al., 2007) whereby slow movements (of cm/year) along a thin shear band (from cm to m) can trigger mechanical dissipation that increases the temperature and reduces the shearing resistance of the material inside the shear band (Anderson, 1980; Lachenbruch, 1980; Mase & Smith, 1984; Rice, 2006; Vardoulakis, 2002b; Voight & Faust, 1982). This process (positive thermal feedback loop) can continue up to the point when the friction coefficient decreases uncontrollably due to a thermal runaway instability (Gruntfest, 1963), even without any variations of external factors (i.e., loading conditions).

Over the years, several authors have focused on such behavior of the shear band and presented models of its thermo-poro-mechanical response during slip, especially with clays as the material present in the gouge (Alonso et al., 2016; Cecinato & Zervos, 2012; Goren & Aharonov, 2007, 2009; Goren et al., 2010; Pinyol & Alonso, 2010; Vardoulakis, 2002b; Veveakis et al., 2007). This paper is also part of an attempt to constrain further the combination of internal factors (which change the material's friction coefficient, like thermal softening) and the temporal variations of external factors (which drive the shear stress, like groundwater fluctuations) to provide a time-dependent assessment tool for deep-seated landslides. Hence, we generalize the analysis of Veveakis et al. (2007), taking into account the groundwater variations. Although the previous study of Veveakis et al. (2007) has produced some stability regimes for the response of the material (internal factors) by isolating the material's internal response from the influence of external factors, it does not provide any information on the role of external stress variations. Indeed, the analysis of Veveakis et al. (2007) was performed under constant loading stress, that is, neglecting the effects of transient precipitation or groundwater variations. In this work, we generalize these concepts and study the internal response of the material subjected to a transient groundwater level. By doing so, we aim at providing a kinematic (time-dependent) stability criterion that couples the external forcing of a landslide (i.e., groundwater variations in this case) with its internal response as this was studied by Veveakis et al. (2007).

For this analysis, we consider two case studies: the Vaiont landslide (Italy) and the Shuping landslide (Three Gorges Dam, China). For the Vaiont slide, we study the two years of creep until its collapse, reproducing the velocity history as provided by Muller (1964, 1968). Similarly, in the case of the Shuping landslide, we study 5 years of its creeping phase (remaining active nowadays), reproducing the velocity history retrieved from Huang et al. (2014). We have chosen these two landslides as characteristic examples of large deep-seated landslides that have been very well documented. The common characteristics that these two large deep-seated landslides share are (1) their shear bands are formed by clays (thereby expecting similar response to variations of internal factors like temperature), and (2) they are ancient landslides that reactivated upon the construction of a dam in their vicinity. However, their main difference is their response to the reservoir variations (i.e., to external factors), since the Vaiont landslide accelerated when the reservoir level increased, while Shuping stabilizes when the reservoir level rises. Therefore, the two landslides seem to have an opposite internal response to similar external stimulation (variations of the groundwater), allowing for an in-depth assessment of the limitations of our approach.

2. Multi-Scale Model of a Deep-Seated Landslide

The multiscale model for deep-seated landslides presented in this study incorporates three configurations at two scales, as initially suggested by Vardoulakis (2002a) and shown in Figure 1. The mathematical equations of the problem include the momentum, mass, and energy balance laws [see also Rice, 2006]:

SEGUÍ ET AL. 2 of 24

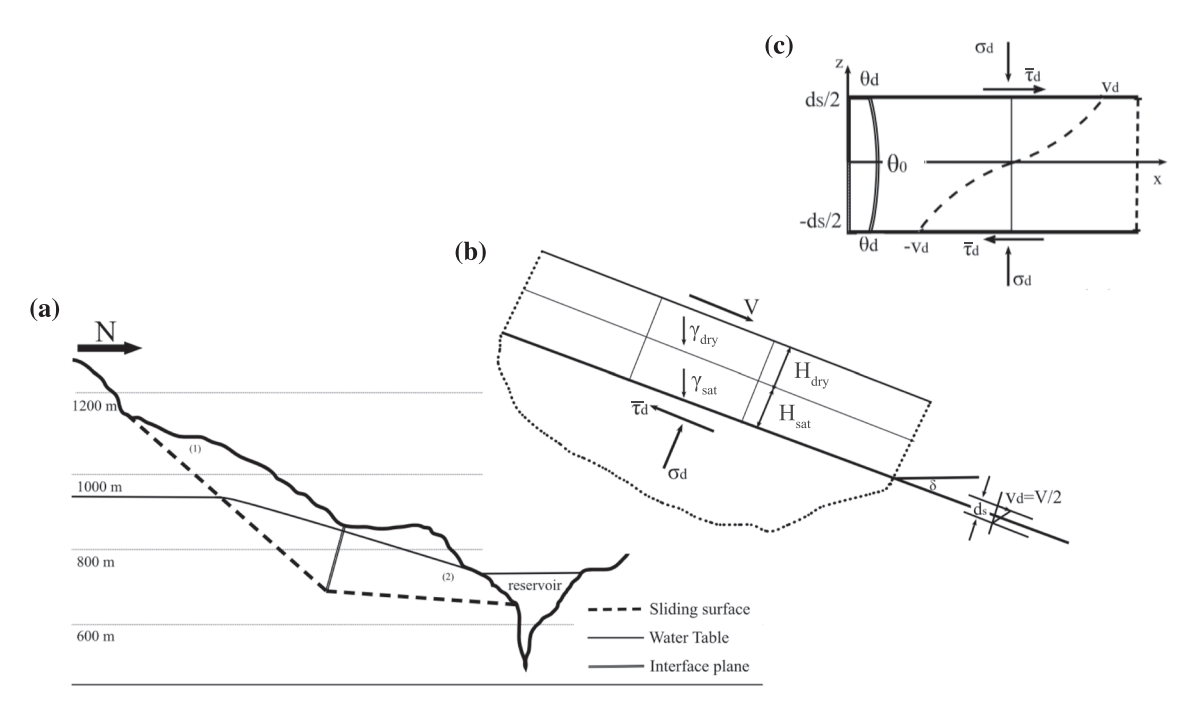


Figure 1. Multiscale model of a deep-seated landslide. (a) Static configuration: Topographic cross section of the landslide in which classical stress calculations are performed. (b) Kinematic configuration: The landslide is treated as translational, with its kinematics represented as an infinite rigid-elastic block sliding over a shear band, where $\bar{\tau}_d$ is the mean basal shear stress, σ_d is the normal force, γ_{dry} is the specific unit weight of the dry material, γ_{sat} is the specific unit weight of the saturated material, γ_{sat} is an average of the height of the saturated material, γ_{sat} is the angle of the shear band with the horizontal, γ_{sat} is the shear band thickness, and γ_{sat} is the velocity. (c) Shear band configuration: The shear band of the landslide incorporating thermo-mechanical couplings (Veveakis et al., 2007), where γ_{sat} is the temperature.

$$\operatorname{div}(\boldsymbol{\sigma}) + \rho g = \rho \frac{\partial V}{\partial t} \tag{1}$$

$$\frac{\partial p}{\partial t} + V \nabla p = D_m \nabla^2 p + \Lambda \frac{\partial \theta}{\partial t} - \frac{\dot{\varepsilon}^i}{\beta}$$
 (2)

$$\frac{\partial \theta}{\partial t} + V \nabla \theta = \kappa_m \, \nabla^2 \theta + \frac{\tau \dot{\gamma}^i + \sigma' \dot{\varepsilon}^i}{\rho C_m} \tag{3}$$

combined with appropriate constitutive equations, at both scales. In these expressions σ is the total stress tensor; ρ is the density of the material; V the velocity; p is the total pore pressure, consisting of a hydrostatic and an excess part; D_m is the hydraulic diffusivity; β is the mixture's compressibility; θ is the temperature; Λ is the thermal pressurization coefficient; κ_m is the thermal diffusivity; C_m is the specific heat capacity; $\tau \dot{\gamma}^i + \sigma' \dot{\varepsilon}^i$ is the total dissipation consisting of a deviatoric $(\tau \dot{\gamma}^i)$ and a volumetric $(\sigma' \dot{\varepsilon}^i)$ part. $\dot{\gamma}^i$ are the irreversible parts of the deviatoric and volumetric strain rates, respectively. τ and σ' are the deviatoric and volumetric parts of the effective stress tensor, respectively. The Terzaghi effective stress tensor is linked to the total stress tensor by $\sigma' = \sigma + pI$ (compression negative) assuming for simplicity that solid matrix is incompressible. However, as explained in detail by Veveakis et al. (2007), because of the vastly different length scales of the overburden mass (tens to hundreds of meters thick) and the sliding surface (a few centimeters thick, also called shear band in this study), it is possible to separate the physical processes operating at each scale.

Indeed, the overburden is treated as a rigid block (i.e., admitting no internal deformation $\dot{\gamma}^i = \dot{\epsilon}^i = 0$), with the only source of deformation (and thus heat production) being the interface with the sliding surface. In addition, we consider here the case of creeping landslides with no significant internal mass and heat

SEGUÍ ET AL. 3 of 24



advection processes (i.e., involving materials like clays, having negligible permeability of the order of microDarcy or less), thereby eliminating acceleration and advective terms. Under these assumptions, the validity of which will be also discussed in section 6, the equations for the overburden reduce to

$$\operatorname{div}(\boldsymbol{\sigma}) + \rho g = 0 \tag{4}$$

$$\frac{\partial p}{\partial t} = D_m \nabla^2 p + \Lambda \frac{\partial \theta}{\partial t}; \quad \frac{\partial \theta}{\partial t} = \kappa_m \nabla^2 \theta \tag{5}$$

The obvious solution to the pore pressure and temperature diffusion equations is considering the trivial solution of constant fields ($\theta = \text{const.}$, p = const.). This is true for the temperature, when external heating sources are not present (i.e., when isothermal boundary conditions are assumed). However, since the pore pressure can vary with externally imposed hydraulic head variations (recall that the hydraulic head h for a given elevation of the piezometric bottom Y is equal to $h = \frac{p}{\rho g} + Y$), it cannot be assumed constant. The final equations of the overburden therefore consist of the stress equilibrium and pressure (or equivalently hydraulic head) diffusion equations:

$$\operatorname{div}(\boldsymbol{\sigma}) + \rho g = 0 \; ; \; \frac{\partial h}{\partial t} = D \frac{\partial^2 h}{\partial x^2}$$
 (6)

where D is the diffusivity constant $(D = D_m/H)$.

Unlike the overburden, the shear band is considered fully saturated in water, deformable, and viscoplastic. However, its very small thickness compared to its length has twofold ramifications: first, it reduces the equations in essentially 1D inside the shear band, with all the fields varying only across the z direction of the shear band (Figure 1); and second, it eliminates any effect of gravity or inertia, as well as any changes of the hydrostatic pressure inside the shear band (Rice, 2006; Vardoulakis, 2002b; Veveakis et al., 2007). This reduces the momentum balance equations to constant stresses inside the sliding surface and—together with the assumption of negligible advection inside the shear band—reduces the system of equations to

$$\frac{\partial \sigma_{xz}}{\partial z} = 0 \to \sigma_{xz} = \tau_d(t); \frac{\partial \sigma_{zz}}{\partial z} = 0 \to \sigma_{zz} = \sigma_n(t)$$
 (7a)

$$\frac{\partial \Delta p}{\partial t} = D_m \frac{\partial^2 \Delta p}{\partial z^2} + \Lambda \frac{\partial \theta}{\partial t} - \frac{\dot{\varepsilon}^i}{\beta} \tag{7b}$$

$$\frac{\partial \theta}{\partial t} = \kappa_m \frac{\partial^2 \theta}{\partial z^2} + \frac{\sigma_{xz} \dot{\gamma}^i + \sigma'_{zz} \dot{\varepsilon}^i}{\rho C_m}$$
 (7c)

In these expressions, Δp is the value of excess pore water pressure inside the sliding surface ($\Delta p=0$ at the boundary ensuring drained conditions), and $\tau_d(t)$ and $\sigma_n(t)$ are the values of the (time-dependent) shear and normal stresses applied on the sliding surface's boundary, which is also the interface between the sliding surface and the overburden. Note that the condition $\sigma_{zz}=\sigma_n(t)$ can also be written for the effective stresses as $\sigma'_{zz}-p_{\rm hydrostatic}-\Delta p=\sigma_n(t)$ (where the pore fluid pressure is split into a hydrostatic and an excess part) or equivalently $\sigma'_{zz}=\sigma'_n(t)+\Delta p$. The two scales communicate through this common boundary, on which continuity of the fields (stresses, pore pressure, and temperature) needs to be ensured. However, the fact that the equations of the sliding surface are 1D and those of the overburden 2D, for every cross section of a landslide, causes the need for an additional mathematical/configurational step where the calculations of the two domains are linked together in an equivalent topography.

This is achieved as shown in Figure 1, by considering three configurations: (a) a *static configuration*, in which the topography enables us to calculate the groundwater table and therefore the shear stress applied along the sliding surface of the landslide. To do so, in this 2D configuration we are solving the equation of the overburden, Equation 6, thereby calculating the stresses acting on the real (2D) sliding surface; (b) a *kinematic configuration*, in which the landslide topography is mapped to an equivalent rigid block geometry sliding on a surface. In these configurations, the stresses acting on the 2D sliding surface are mapped into an

SEGUÍ ET AL. 4 of 24



equivalent 1D configuration, and the displacement of the block (Figure 1b) is calculated from the geometry and the stresses determined in the static configuration (Figure 1a); and (c) the *shear-band configuration*, in which a smaller scale is considered, represents the sliding surface where its kinematic configuration is modeled as an infinite sheared layer (in dimensionless form) and includes the multiphysical phenomena happening in this thin zone. Moreover, in this configuration (Figure 1c) we are solving the equations of the sliding surface (Equation 7).

Note that the above considerations and assumptions imply that the present study focuses only on (1) translational landslides, since the kinematic configuration is an infinite plane; and (2) thermo-poro-mechanical behavior of the material in the shear band. The following paragraphs present in more detail how each configuration of the multiscale model is approached and linked to one another.

2.1. Groundwater Table of a Landslide

As a first step, we calculate the stresses and their evolution acting along the sliding surface, through a hydro-mechanical analysis of the landslide (at the static configuration level). For this calculation we need two elements: (1) the groundwater table and (2) the forces acting inside the landslide (including the sliding mass). Thus, to study the groundwater table of a landslide, we consider the topographic cross section of the scale in Figure 1a and calculate the hydraulic head (h). The hydraulic head is calculated at each point (horizontal distance) of the landslide considering (a) the steady-state solution for the Vaiont landslide (section 4.2) and (b) a transient solution for the Shuping landslide (section 5.2).

2.2. Limit Equilibrium and Coulomb Mechanism of a Landslide

Once the groundwater level of the landslide is determined, we calculate the time-dependent shear stress of the landslide (with time entering through the evolution of the groundwater level), by performing a limit-equilibrium analysis (Figure 2) in the *static configuration* scale in Figure 1a. This static configuration is required to calculate the force values that are acting on the "real shape" of the landslide. To this end, we apply the two-wedge method (Alonso, 1989a and 1989b) to simplify the calculations. The implementation of the two-wedge method requires (1) first, a force equilibrium calculated separately for each wedge, and (2) second, calculate the total shear stress of the landslide acting on the slip plane as a mean of shear stresses acting at the base of each block (Alonso & Pinyol, 2010; Veveakis et al., 2007). Hence, we divide the landslide into two blocks considering the topography of the landslide. To separate the landslide into two blocks, we set the division line: (1) at the point where the sliding surface (i.e., shear band) changes its slope sharply and (2) at the point where the topography changes the slope drastically (Figure 2). It should be noted that the two-wedge method is just one of the available limit equilibrium approaches (others being the Fellenius or Bishop method of slices) and is used in the present study to simplify the mathematical treatment

We consider that Wedge 1 acts on Wedge 2 as an active force, and Wedge 2 acts on Wedge 1 as a passive force, following the basics of the limit equilibrium theory detailed by Craig (Chapter 4, 2004). This consideration takes into account the slopes of the shear band of each wedge. Thus, the wedge that has the higher shear band's slope acts actively, and the wedge that has a lower shear band's slope acts passively. Applying the limit equilibrium analysis, detailed in Appendix A, in the double-wedge structure (see also Chapters 11–12 of Craig, 2004), we calculate the mean basal shear stress force for the landslide as

$$\bar{\tau}_{\rm d} = \frac{1}{H^{(1)} + H^{(2)}} \left(H^{(1)} \tau_{\rm d}^{(1)} + H^{(2)} \tau_{\rm d}^{(2)} \right) \tag{8}$$

In Equation 8, $\bar{\tau}_{\rm d}$ is the mean shear stress of the landslide (acting on the sliding surface), $H^{(1)}$ is an average height of dry soil height plus saturated soil height of Wedge 1, $\tau_{\rm d}^{(1)}$ is the shear stress of Wedge 1 (at the shear band of Wedge 1), $H^{(2)}$ is an average height of dry soil height plus saturated soil height of Wedge 2, and $\tau_{\rm d}^{(2)}$ is the shear stress of Wedge 2 (at the shear band of Wedge 2). Note that the dry and saturated soil heights of each wedge have been calculated from the areas obtained at each groundwater level.

SEGUÍ ET AL. 5 of 24



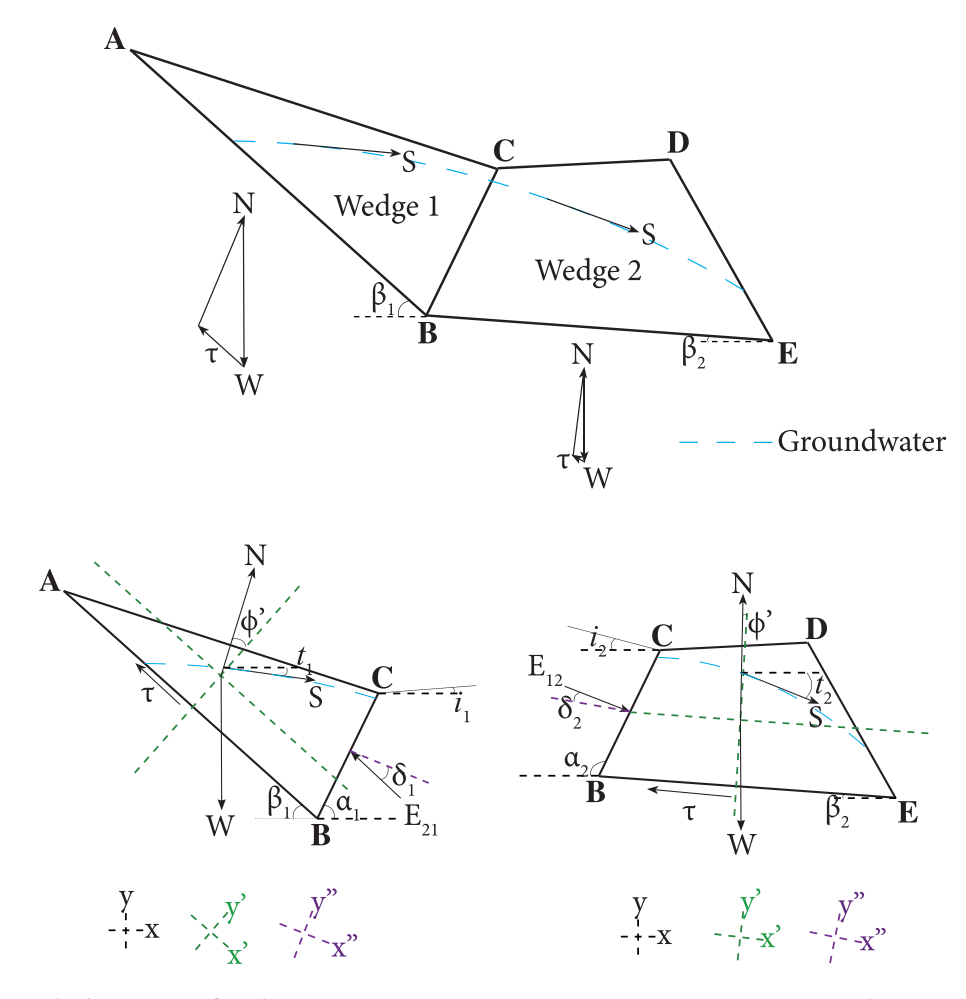


Figure 2. (top) Section profile of a deep-seated landslide with a two-wedge mechanism and its force equilibrium. (bottom) The forces acting on each of the two wedges, where N is the normal force, S is the seepage force, W is the weight, τ is the shear stress, and E_{12} and E_{21} are the lateral pressures.

2.3. Thermo-Poro-Mechanical Behavior of the Shear Band

After calculating the forces acting on the landslide, we consider that the slide will kinematically evolve as a translational landslide, being thereby able to be represented by a simple 1D rigid-block/shear-band configuration (Figure 1b). We briefly present the conceptual model used in the paper of Veveakis et al. (2007) to describe such a deep-seated landslide, incorporating the kinematic configuration and *shear-band configuration* scales, as shown in Figures 1b and 1c. As such, a translational landslide is considered as an infinite rigid-elastic block sliding over a thin (order of centimeter) layer of clay (i.e., the sliding surface or shear band). The slope where the infinite rigid-elastic block is sliding has been considered as a mean between

the slopes of the two wedges of the landslide (calculated as $\frac{\beta_1+\beta_2}{2}$) so that the dynamics of the landslide is respected. As we assume that the block is rigid, its vertical velocity (direction perpendicular to the sliding surface) is constant. The rigid-elastic block, therefore, admits the shear stresses (calculated in the previous section 2.2) at its basal interface and, because we consider that the contact between the base of the infinite rigid-elastic block (Figure 1b) and the shear band is continuous (Figure 1c), the same shear stress is also transferred on the shear band.

We recall that the equations of the shear band are Equations 7a–7c, which require a constitutive law for the mechanical response of the basal material to obtain a mathematically closed system of equations. We start by

invoking the definition of dilatancy $\psi=rac{\dot{arepsilon}^i}{\dot{\gamma}^i}$ to have Equations 7a–7c written as

SEGUÍ ET AL. 6 of 24

$$\frac{\partial \Delta p}{\partial t} = D_m \frac{\partial^2 \Delta p}{\partial z^2} + \Lambda \frac{\partial \theta}{\partial t} - \psi \frac{\dot{\gamma}^i}{\beta}$$
(9a)

$$\frac{\partial \theta}{\partial t} = \kappa_m \frac{\partial^2 \theta}{\partial z^2} + \left(\frac{\tau_d + \sigma'_n \psi + \Delta p \, \psi}{\rho C_m} \right) \dot{\gamma}^i \tag{9b}$$

Based on the assumption that the landslides we are going to be modeling in this work are reactivated, and the fact that clays reach critical state (deforming under constant volume, i.e., zero dilatancy) upon relatively small displacements when sheared (Tika & Hutchinson, 1999), we assume that the clay material inside the shear zone is at critical state for every variation of the groundwater table. This assumption implies that $\psi=0$, and any volumetric effect is negligible (see also Rice, 2006), therefore eliminating the possibility of the model generating excess pore fluid pressure due to volume change effects (Garagash & Rudnicki, 2003; Iverson, 2005; Veveakis & Regenauer-Lieb, 2015). This is obviously a strong assumption and limitation of the present model, which will be reassessed for its validity in section 6.

In addition to the above, although thermal pressurization is still a plausible mechanism inside the shear band, Veveakis et al. (2007) showed that it is triggered once the basal temperature exceeds a certain value (for clays the critical temperature is of the order of 40 °C), something that is achieved only at the very last stages of the landslide failure, when catastrophic acceleration takes place (Cecinato et al., 2011; Vardoulakis, 2002a; Veveakis et al., 2007). This, in turn, means that during the prolonged slow creeping phase the equations are reduced to the temperature equation 9b, requiring a constitutive response for the irreversible part of the strain-rate $\dot{\gamma}^i$.

This is obtained by assuming the behavior of the clay material inside the shear zone to be viscoplastic ($\dot{\gamma}^i = \gamma$), exhibiting thermal and rate sensitivity, following the work of Vardoulakis (2002b). Hence, we assume (1) *velocity hardening* (the strain-rate increases when increasing the shear stress) and (2) *thermal softening* (when the temperature of clays increases, the friction coefficient of the material decreases). As discussed in the seminal work of Vardoulakis (2002b) and briefed by Veveakis et al. (2007) and Cecinato et al. (2011), these two mechanisms are supported by experimental data on clays (Hueckel & Baldi, 1990). Additional mechanisms that could affect the shearing resistance of the material inside the shear band can be considered, such as strain softening (Vardoulakis, 2002a) and rate softening (Handwerger et al., 2016). It was argued by Veveakis et al. (2010) that rate softening accommodated with thermal (or any other) hardening would have the same result in the frictional response of the basal material, as the only requirement for a stable creeping phase is that the operating mechanisms can counterbalance each other, so that the shearing resistance (i.e., friction coefficient) of the material can attain a constant (critical state) value. For this reason strain softening is not included, as it would automatically drive the system away from critical state and toward a residual value of the shearing resistance.

The shearing resistance (friction coefficient) at critical state can therefore be defined as a product of (1) a power law dependency for the velocity $[g(\dot{\gamma})]$ and (2) an exponential thermal softening $[f(\theta)]$:

$$\mu_{\rm cs} = g(\dot{\gamma}) \cdot f(\theta) = \mu_{\rm ref} \left(\frac{\dot{\gamma}}{\dot{\gamma}_{\rm ref}} \right)^N e^{-M(\theta - \theta_1)} \tag{10}$$

where $g(\dot{\gamma})$ is the velocity hardening of clays expressed as $\left(\frac{\dot{\gamma}}{\dot{\gamma}_{\rm ref}}\right)^N$ and $f(\theta)$ is the thermal softening of clays

defined as $e^{-M(\theta-\theta_1)}$. In this expression, $\mu_{\rm cs}$ is the friction coefficient at critical state, $\mu_{\rm ref}$ is the reference friction coefficient, $\dot{\gamma}$ is the shear strain-rate, N is the frictional rate-sensitivity coefficient, M is the frictional thermal-sensitivity coefficient, θ_1 is the reference (boundary) temperature, and θ is the actual temperature in the shear band.

Considering that the shearing resistance at critical state is defined as $\mu_{\rm cs} = \frac{\tau_d}{\sigma'_n}$ (where τ_d is the shear stress and σ'_n is the effective normal stress), we can solve Equation 10 for the strain-rate $\dot{\gamma}$ and obtain the following expression:

SEGUÍ ET AL. 7 of 24



$$\dot{\gamma} = \frac{\partial V}{\partial z} = \dot{\gamma}_{\text{ref}} \left(\frac{\tau_d}{\tau_{\text{ref}}}\right)^{1/N} e^{m(\theta - \theta_1)}, \text{ where } \tau_{\text{ref}} = \mu_{\text{ref}} \ \sigma'_n; \ m = \frac{M}{N}$$
 (11)

In this expression, m is the exponent ratio of the temperature sensitivity coefficient [M] over the strain-rate sensitivity coefficient [N]. Note that the dependency on the temperature $[\theta]$ with an exponential law (Equations 10 and 11) corresponds to the low-temperature approximation of the more generic Arrhenius law. This law has also been used in the field of fault mechanics (Alevizos et al., 2014; Poulet et al., 2014; Veveakis et al., 2014).

Having established the constitutive law for the basal material (velocity hardening and thermal softening of clays at critical state), we combine Equation 11 with Equation 9, so that the final equation of the shear band reads:

$$\frac{\partial \theta}{\partial t} = \kappa_m \frac{\partial^2 \theta}{\partial z^2} + \left(\frac{\tau_d}{\rho C_m}\right) \dot{\gamma}_{\text{ref}} \left(\frac{\tau_d}{\tau_{\text{ref}}}\right)^{1/N} e^{m(\theta - \theta_1)}$$
(12)

with boundary conditions $\theta = \theta_1$ at $z = -\frac{ds}{2}, \frac{ds}{2}$.

Equation 12 can be reduced in a single-parameter dimensionless equation

$$\frac{\partial \theta^*}{\partial t^*} = \frac{\partial^2 \theta^*}{\partial z^{*2}} + Gr \, e^{\theta^*}, \quad z \in [-1, 1], \, t > 0$$

$$\tag{13}$$

by using the following dimensionless parameters:

$$z^* = \frac{z}{\left(\frac{ds}{2}\right)}, \qquad t^* = \frac{\kappa_m}{\left(\frac{ds}{2}\right)^2} t, \quad \theta^* = m(\theta - \theta_1)$$
 (14)

where ds is the thickness of the shear band (represented in Figure 1c), and Gr is the so-called Gruntfest number (Gruntfest, 1963), defined as follows:

$$Gr = m \frac{\dot{\gamma}_{\text{ref}}}{F_{\theta}} \left(\frac{ds}{2}\right)^{2} \tau_{\text{ref}} \left(\frac{\tau_{d}}{\tau_{\text{ref}}}\right)^{1+1/N} \tag{15}$$

where F_{θ} is the thermal conductivity ($F_{\theta} = \kappa_m \rho C_m$) and $\tau_d = \bar{\tau}_d$ is the basal mean shear stress of the landslide (Equation 8) calculated for each groundwater level. The Gruntfest number (Gr) expresses the ratio of the mechanical work converted into heat over the heat diffusion capabilities of the material. This parameter includes all the material properties at hand (thermal conductivity, rate and thermal sensitivities, and reference rate), as well as the thickness of the shear band and the normal and shear stresses applied in the shear band's material. Since these stresses (normal and shear), which are calculated in the previous section (2.2), evolve with the groundwater level (section 2.1), Gr is expressing the influence of *external loading* on the shear band and is therefore not constant in time. This is distinctly different than the approach adopted by Veveakis et al. (2007) where the loading stresses were constant.

3. Stability Analysis of a Deep-Seated Landslide

Having established the governing equation of the shear band (Equation 13), we need to assess the regions of stability of the system. The stability assessment of the system is achieved by performing a numerical bifurcation analysis of the steady-state:

$$\frac{\partial^2 \theta^*}{\partial z^{*2}} + \operatorname{Gr} e^{\theta^*} = 0, \tag{16}$$

The numerical bifurcation analysis is performed with respect to the only parameter of the system, *Gr*, by using a pseudo-arc-length continuation approach (Chan & Keller, 1991; Veveakis et al., 2010).

SEGUÍ ET AL. 8 of 24

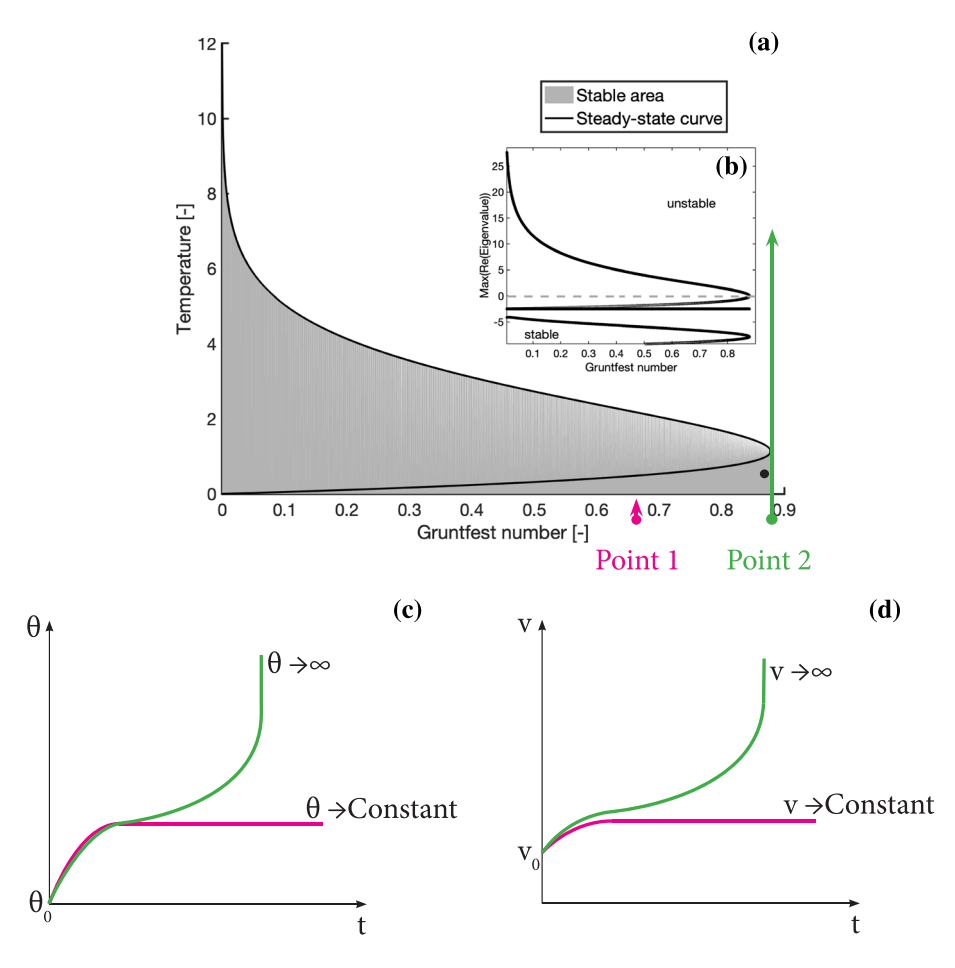


Figure 3. (a) Steady state curve with its critical point (black dot) and the corresponding maximum eigenvalue (inlet b). A stable Point 1 (pink dot) and an unstable Point 2 (green point) are highlighted. The pink and green arrows represent the evolution in time of the system with an initial state described by Points 1 and 2, respectively. (c) Representation of the temperature evolution in time starting from the stable and unstable points from Figure 3a. (d) Representation of the velocity evolution in time starting from the stable and unstable points from Figure 3a.

3.1. Numerical Bifurcation Analysis

Figure 3a presents the results of the numerical bifurcation analysis. This graph expresses the steady-state response of the dimensionless temperature as a function of the Gruntfest number (bifurcation parameter). This bifurcation diagram can be interpreted as follows:

The peak of the steady-state curve (black dot in Figure 3a) is what we call the *critical value of Gruntfest number*, Gr_c . In our system, the results show $Gr_c \sim 0.88$. This critical value defines a limit between two regions of the diagram:

- 1. when $Gr > Gr_c$ (green point of Figure 3a), there is no steady-state solution. Therefore, the system becomes unstable (i.e., the landslide will fail).
- 2. when $Gr \leq Gr_c$, there are two steady-state solutions, expressed as the two branches of Figure 3a. By inspecting the sign of the maximum eigenvalue of the system's Jacobian (Figure 3b), we conclude that the lower branch of the steady state-curve is stable, thereby behaving as an attractor of the transient system, whereas the upper branch is an unstable repeller (see also Veveakis et al., 2010).

Therefore, the steady-state curve delimits the stable area of our system (highlighted as the gray area of Figure 3a). If the system is somehow pushed outside this area (stable area of the system), a catastrophic increase of the temperature will occur, a response known in the literature as thermal runaway (Gruntfest, 1963) or thermal blow-up instability (Veveakis et al., 2007). Since in the present study the

SEGUÍ ET AL. 9 of 24



Gruntfest number represents the shear stress τ_d applied on the sliding surface, which in turn is calculated by the groundwater level through Equation 8, this bifurcation diagram implies that when the groundwater level variations cause the shear stress to increase, Gr number increases and the system is pushed toward its critical value Gr_c . During this motion, the temperature of the shear band can increase due to friction. As long as the combination of shear stress/Gruntfest number and maximum temperature remains in the gray area of Figure 3a, the system has the capacity to diffuse away all the heat generated inside the shear band due to friction and maintain a stable—slow creeping—steady-state. As soon as the stress (i.e., Gr) or temperature increases above (or outside) the upper branch of the curve and the system is pushed to the white area, the system is entering a quasi-adiabatic regime, where the temperature generated due to friction cannot be diffused away by the material, and causes abrupt increase of the temperature, in a process known as thermal runaway.

To better understand the system's behavior, in terms of transient temperature and velocity inside the shear band, we have selected two example points in Figure 3a and examine the response of the system from these initial conditions (Point 1 and Point 2 in Figure 3a). If the system is at an initial state represented by Point 1 (pink dot in Figure 3a), which corresponds to a Gruntfest value below Gr_c , the temperature and velocity of the system tend to reach a steady value (pink curves in Figures 3c and 3d). This means that when the Gruntfest number is located below the turning point, the landslide would creep stably. However, if the system is at an initial state represented by Point 2 (green point in Figure 3a), corresponding to a Gruntfest value above Gr_c , the temperature and velocity would increase exponentially (i.e., blow-up) over time (green curves in Figures 3c and 3d), meaning that the landslide would collapse catastrophically in a finite time. The bifurcation diagram of Figure 3a can therefore be viewed in light of an operational protocol, with the gray area where $Gr \leq Gr_c$ holds true delimiting the values of the shear stresses (and hence of the groundwater level) a slope can admit without failing catastrophically.

3.2. Procedure for the Inversion of Field Case Studies

This analysis, thus, highlights the crucial role of the Gruntfest number in the stability of the system, suggesting that Gr is the bifurcating parameter for the stability of a landslide. As already discussed, Gr is not constant over time, as the loading conditions (shear stress) of the landslide are included in the Gruntfest number. Using the definition of the Gruntfest number (Equation 15), and the values of the shear stress calculated by the groundwater analysis (Equation 8), we will test whether the stability threshold of a landslide can be indeed evaluated through the bifurcation analysis presented in this section. In the next sections we apply the model to two case studies with different behaviors: (1) the Vaiont landslide in Italy, which turned unstable after years of slow creep and failed catastrophically; and (2) the Shuping landslide in China, which has been creeping stably for decades.

We note that the system depends on a single parameter, as Gr is the only number that determines the response of the mathematical system of equations (i.e., the response of the clay material—inside the shear band—under external loading). As Gr is a dimensionless group of parameters, it encompasses several of the material's properties and loading conditions. In the following examples, we start by bringing the velocity data provided in the field (through Global Positioning System stations) in a dimensionless form using the definition of the dimensionless time and space of Equation 14. To do so, we start by inputting the values of thermal properties (thermal conductivity and diffusivity), which do not vary significantly across all Earth materials, as well as the shear band thickness of each landslide that is reported in the literature. Having normalized the field data (displacement/velocity and time), we proceed by fitting them with our model, using the time-dependent Gr number as an inversion parameter.

Through this inversion process we obtain optimal values of Gr and the rate sensitivity N (which governs the response of the velocity of the model with respect to shear stress variations and therefore groundwater level variations), as well as the initial conditions for the shear stress and strain-rate (calculated as initial velocity over shear band half-thickness). Our final step is to use this value of Gr, the value of N, and the initial value of the stress to infer the thermal sensitivity coefficient M and the reference strain-rate $[\dot{\gamma}_{ref}]$. It is to be noted that, although representative values have been given for N and M by Veveakis et al. (2007) based on generic literature data of clays (Leinenkugel, 1976) and simple models assessing the dependence of water viscosity on temperature (Bagnold, 1954; Veveakis et al., 2007), these parameters are material sensitive and can only be determined through material testing at different rates and temperatures. Because of the nonlinear

SEGUÍ ET AL. 10 of 24



Table 1
Material Parameters of the gouge of Vaiont and Shuping (Li, 2015; Veveakis et al., 2007) landslides

Parameter	Vaiont Value	Shuping Value	Units	Range	Source
ds	0.161	0.7	m	0.2-0.0015	Veveakis et al. (2007), Vardoulakis (2002a) for Vaiont
κ_m jk_m $\dot{\gamma}_{ref 1}$	$1.6 \cdot 10^{-7}$ 0.45 $1.7 \cdot 10^{-2}$	$1.6 \cdot 10^{-7}$ 0.45 $4.9 \cdot 10^{-2}$	$J ({}^{\circ}C \underset{s}{m} \underset{s}{s})^{-1}$	$0.6-1.0 \\ 10^{-7}-10^{-6} \\ 0.1-1$	Wu et al. (2018) for Shuping Picard (1994) Vardoulakis (2002a) Parameter fitted in the model
γ ref 1 γ _{ref 2}	$3.4\cdot 10^{-2}$		s^{-1}		Parameter fitted in the model
N	0.01	0.025	[-]	0-1	Veveakis et al. (2007)
M	0.0093	0.0093	$^{\circ}\mathrm{C}^{-1}$	0 - 1	Vardoulakis (2002a),
$ heta_1$	22	-	°C		Veveakis et al. (2007)
D	-	2.5	m/s	0.01-2.5	Li (2015)

dependence of Gr on them, the model is extremely sensitive to small variations of their values (especially N). The parameters used both as input and output of the model for the case studies of this work are listed in Table 1 and will be further discussed in section 6.

4. Case Study: Vaiont Landslide

The famous Vaiont landslide (Figures 4a and 4b) failed on October 9th of 1963, in Northern Italy. It has been reported in the literature as an ancient landslide that reactivated when the water level increased in the reservoir (in 1959) after the construction of the Vaiont dam (Semenza & Melidoro, 1992). As such, in this work we will assume that the landslide is a reactivation of an ancient landslide, allowing us to consider the basal material at critical state and deploy the suggested framework.

During the three years of creeping phase of the landslide, the reservoir level fluctuated depending on the season of the year, with heights from 590 to 710 m (Figure 4e) (Muller1964, 1968). Since the landslide was instrumented, it had been seen that the velocity of the slide increased when the lake level rose (Figure 4e). Therefore, the landslide was stabilized by controlling the reservoir level. However, on September 1st of 1963, the reservoir's level reached 710 m and the slide started accelerating, and although the reservoir's level was reduced on October 2nd of 1963, to stop the acceleration, the landslide accelerated until failure (Muller1964, 1968). The average thickness of the sliding mass was about 150 m involving a volume of rock of 2.7×10^8 m³ (Figure 4c) (Muller1964, 1968). When the event occurred, the rock mass slid into the reservoir creating a wave that overflowed the dam and caused approximately 2,000 casualties in the downstream valley.

4.1. Geographical Location and Geological Framework

The Vaiont dam is situated in a steep valley in the Italian Alps, under the Mount Toc in the Pordenone province, region of Friuli-Venice Julia in Northern Italy (Figure 4a). The Piave River crossed this valley ending up in the Vaiont Lake. Upstream, the valley is wide as it was formed by glacial erosion, and downstream the valley is narrower, which made it an appropriate location to place a dam. The stratigraphy of the area (Figure 4d) is composed of massive oolitic calcarenite from the Calcare of Vaiont formation; biocalcarenites and micritic limestone from the Fonzano formation; reddish and gray micrite with ammonites with thin layers of clays from Ammonitico Rosso formation; and intercalations of microcrystalline limestones, calcarenites, and loam from the Calcare of Soccher formation of the Lower Cretaceous (Ferri et al., 2011).

Since the mass of rock was sliding over clay layers, a more detailed information of these clay layers is needed. They are composed of 35 to 80% of a mixture of different types of clays (Ca-montmorillonite, smectite, illite, and vermiculite) with grains of calcite and some traces of quartz (Ferri et al., 2011; Tika & Hutchinson, 1999). These kinds of clays are frequently called "expansive clays," which have properties of low shear strength and swell in the presence of water.

SEGUÍ ET AL. 11 of 24



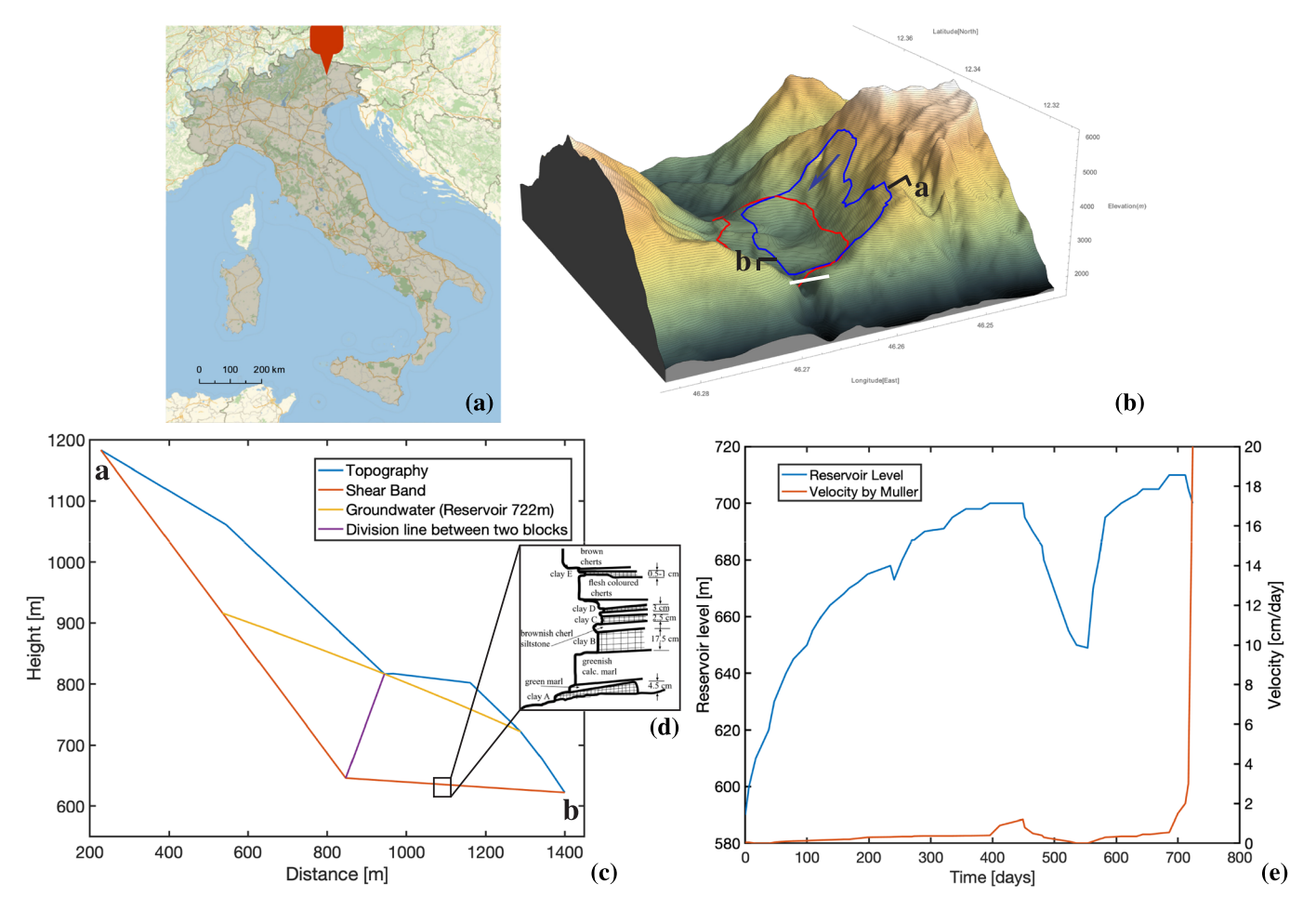


Figure 4. (a) Map of location of the Vaiont dam. (b) 3D elevation map of the Vaiont landslide (the blue line indicates the contour of the initial position of the sliding mass, and the red line its final position after the collapse). The white line shows the position of the dam. (c) Schematic profile of the deep-seated Vaiont landslide. (d) Stratigraphic column of the bottom of the landslide (from Veveakis et al., 2007). (e) Graph showing the reservoir level and the velocity of the landslide during the last two years of recorded data (Muller1964, 1968).

4.2. Groundwater Analysis

The groundwater table evolution of the Vaiont landslide is calculated considering that the dolomite is permeable enough to allow the groundwater to reach a steady-state in between the lake level variations. Thus, we calculate the groundwater level by setting Equation 6 to steady-state, therefore retrieving the Dupuit-Forchheimer parabola as

$$h = \sqrt{U_1^2 - (U_1^2 - U_2^2) \frac{x}{L}}$$
 (17)

where U_1 is the height of the reservoir's level, U_2 is the height of the groundwater table at the fixed point in the back of the landslide (toward the top of the mountain), x is the horizontal coordinate of a point between the two reference points of groundwater level (U_1 and U_2), and L is the horizontal length between the x position of U_1 (the horizontal coordinate of the point of the reservoir's level in contact with the topography of the landslide) and the x position of U_2 (the horizontal coordinate of the fixed point in the back of the landslide).

4.3. Shear Stress Results

To calculate the shear stress of the landslide, we need the data obtained by the groundwater analysis (section 4.2), hence, data from the piezometers. However, in the case of the Vaiont landslide, the data

SEGUÍ ET AL. 12 of 24



provided by the piezometers installed in the landslide are not reliable because of the following issues presented by the four piezometers: (1) the so-called P4 piezometer closed over time due to the displacement of the sliding mass; (2) P1 and P3 piezometers were installed in boreholes whose bottom did not reach the depth of the shear band, for this reason, the groundwater table readings of these two piezometers always presented the same value as the reservoir's level; and (3) P2 piezometer presented values of the groundwater table of approximately 90 m above the reservoir's level. Moreover, in 1962 the borehole where the P2 piezometer was installed also closed due to the displacement of the sliding mass, thus, invalidating the piezometer's readings afterwards. Because of the lack of acceptable data of the piezometers (see Hendron & Patton, 1985 for a further discussion on this topic), this leads us to assume that the landslide is *always* at its maximum capacity of groundwater (for each reservoir's level). This assumption of maximum groundwater capacity of the landslide overestimates the mean basal shear stress by ~0.1 MPa during periods of low precipitation and snowmelt.

Following the double wedge procedure described in Appendix A and using the reservoir's level data of Figure 4e, a linear dependency between the lake level and slip plane shear stresses is obtained. This linear dependency is assumed as the material of the sliding mass (mainly dolomite, mentioned in section 4.2) is considered as a high permeable material, implying that the groundwater behaves as a free aquifer (i.e., the groundwater level fluctuates in parallel to the reservoir's level). This assumption, thus, lets us calculate the shear stress with a simple linear equation that only depends on the reservoir's level (U_1) :

$$\tau_d = 0.0017 \ U_1 - 0.118 \tag{18}$$

where τ_d is the shear stress (MPa), and U_1 is the reservoir level (m). Figure 5a presents the values of the shear stress calculated with Equation 18 for the reservoir levels recorded in the last two years (from 1961 until 1963).

4.4. Transient Stability Analysis

To calculate the velocity of the landslide and the Gruntfest number, the material parameters of the clay inside the shear band of Vaiont are retrieved from Veveakis et al. (2007) (summarized also in Table 1). In the case of the Vaiont landslide, the mathematical system calculated becomes unstable for a value of the Gruntfest number of 0.88 and a maximum dimensionless value of the temperature of 1.2 (Figure 5b). We fit the velocity calculated by our model against the field data (described in Muller, 1964). To match the calculated velocity by our model with the field velocity, we adjust it by applying two values of initial strain-rate. These two values of the strain-rate give two different evolutions of the velocity (Figure 5f), which mark off the limits of the velocity field. This exercise serves as uncertainty quantification, providing a confidence interval for the least constrained parameters like the initial strain-rate.

As shown in Figures 4e and 5f, during the 2 years of recorded data before the collapse of the landslide, the reservoir underwent two large fillings that affected significantly the outcome of the model, in terms of the shear stress, the temperature in the shear band, and the velocity. The fluctuations of the reservoir were performed to stabilize the landslide because the slide accelerated when the reservoir's level increased. However, the last decrease in the reservoir's level could not stop the acceleration of the landslide. Accordingly, we may interpret this last effect through our mathematical model, suggesting that the landslide did not stop its acceleration because the system already out-passed the stability threshold. This implies that the values of the shear stress (i.e., Gruntfest number) and the temperature inside the shear band were already too large (Figure 5b), making impossible to stop the landslide.

Figure 5f shows the results of our model (velocity of the landslide [cm/day] and temperature inside the shear band [°C]) in the case of the Vaiont landslide. The evolution of the temperature inside the shear band shows a parallel behavior to the shear stress and the velocity of the landslide. When the reservoir underwent its first filling, the temperature inside the shear band reached a value of 22.9 °C. And during the second filling of the reservoir, the temperature reached a value between 23.5 and 24 °C. From our model, we found a possible critical value of temperature inside the shear band of 23.5 °C. Hence, we suggest that the landslide collapsed, regardless of the decrease of the reservoir's level after the second filling, because the Gruntfest number (external loading) was increased beyond its critical value, thereby forcing the temperature inside the shear band to overcome its critical value (Figure 5b).

SEGUÍ ET AL. 13 of 24

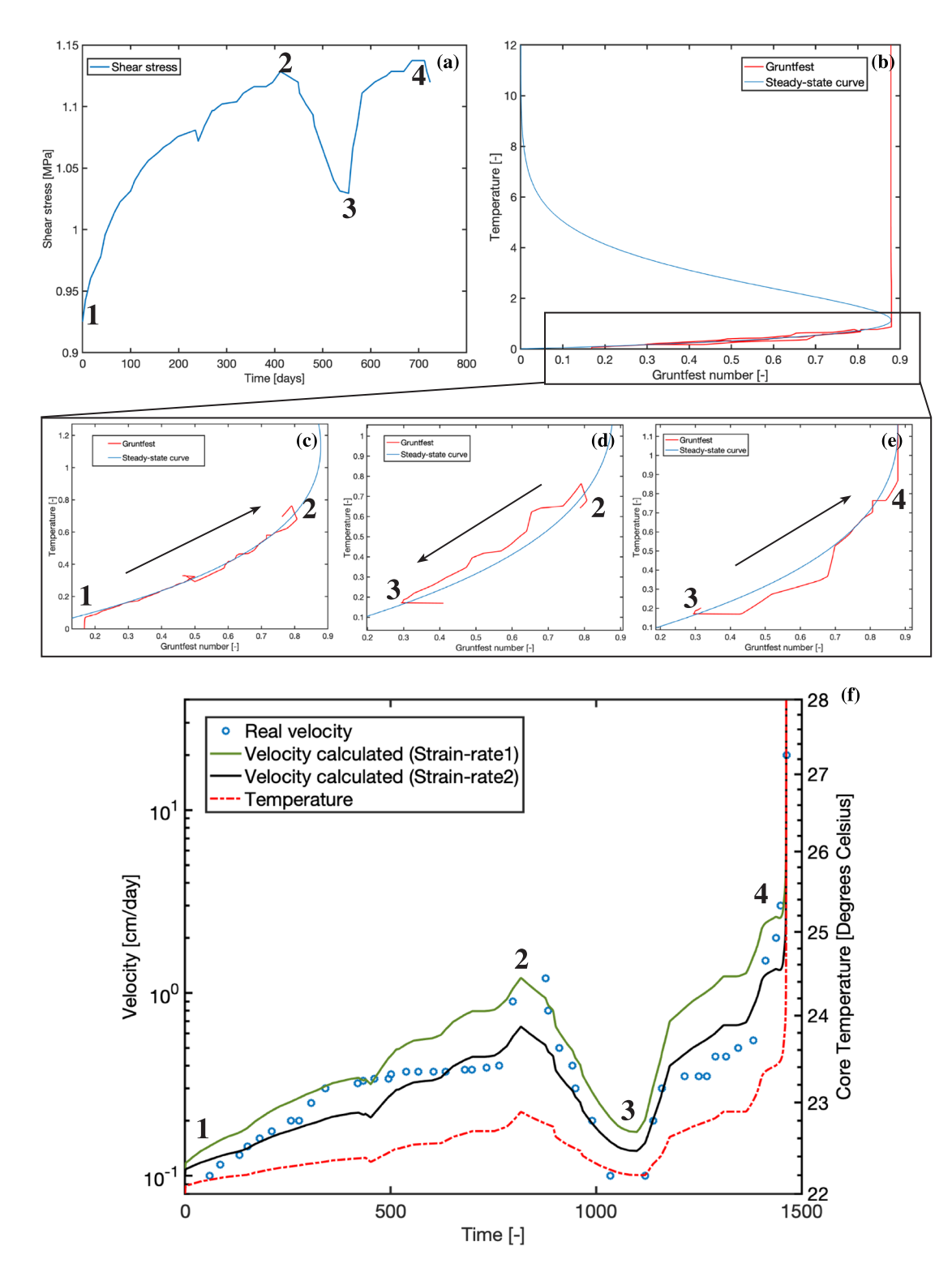


Figure 5. Results of the analysis for the Vaiont slide: (a) Graph representing the shear stress value calculated at each reservoir's level during the last two years of recorded data of the Vaiont dam. (b) Maximum dimensionless temperature inside the shear zone plotted as a function of the Gruntfest number, with the stability curve obtained from the model. (c) Zoom of Figure 5b: for the first filling of the reservoir, Points 1 to 2 of Figure 5a. The arrow represents the direction of the evolution in time of the *Gr* and temperature. (d) Zoom of Figure 5b: for the first reduction of the reservoir, Points 2 to 3 of Figure 5a. (e) Zoom of Figure 5b: for the second and last filling of the reservoir, Points 3 to 4 from Figure 5a. (f) Evolution of the field velocity of the landslide in time (Muller, 1964) as blue dots, and velocity calculated in the model for two different strain-rate values—keeping in mind that $\dot{\gamma} = \frac{\partial V}{\partial z}$ —as green and black lines. The red dashed/dotted line corresponds to the temperature (in time) of the shear band.

SEGUÍ ET AL. 14 of 24

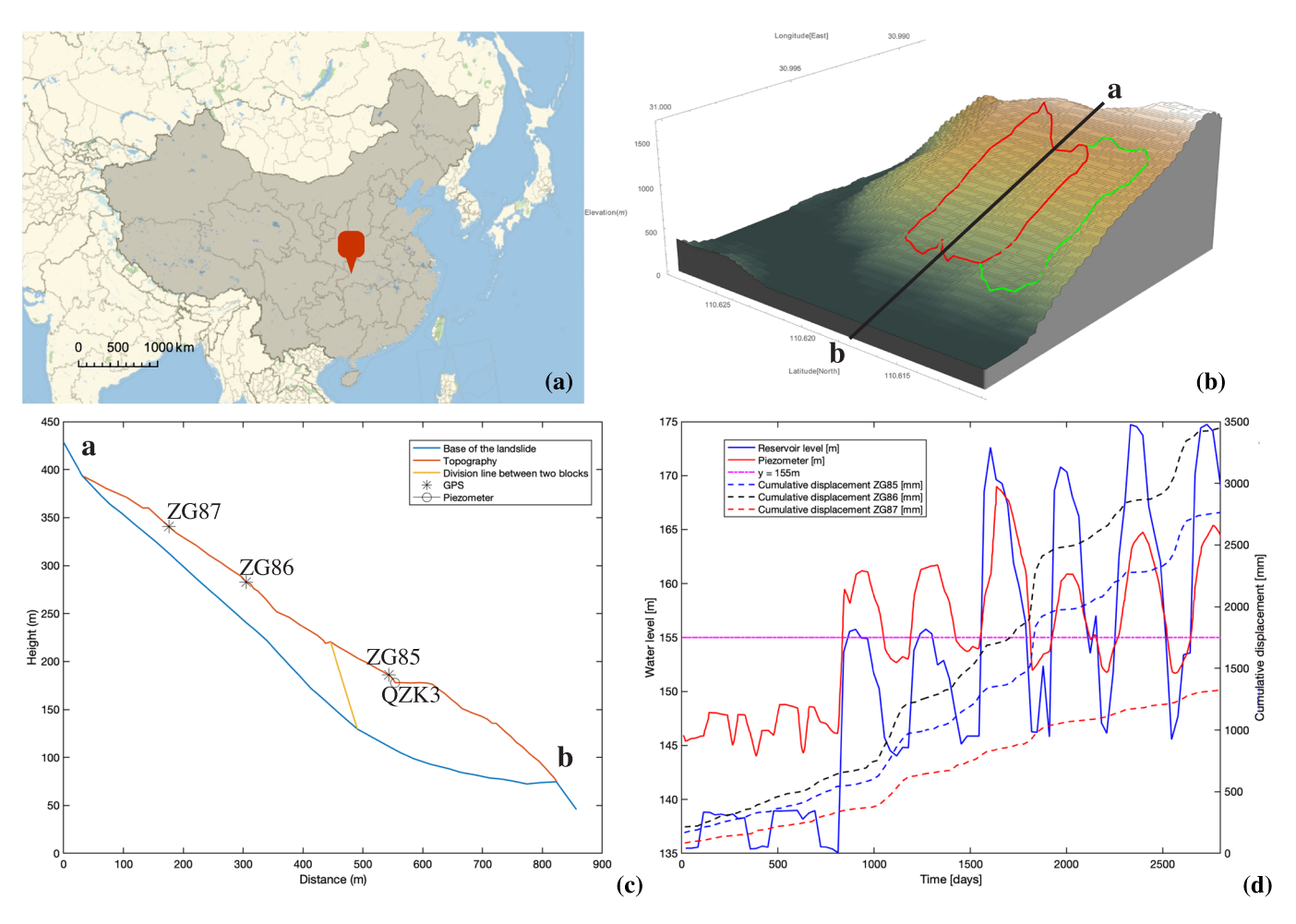


Figure 6. (a) Map of location of the Shuping slide. (b) 3D elevation map of the Shuping landslide (the red line indicates the contour of the active sector of the landslide, and the green line is the dormant sector of the landslide). (c) Profile of the deep-seated Shuping landslide. (d) Graph showing the variations of the reservoir level, the variations of the groundwater level from the piezometer QZK3, the value of reservoir level when there is a zero groundwater slope as magenta dashed line, and the displacement of GPS stations (ZG85, ZG86, and ZG87) of 5 years of recorded data (Huang et al., 2014).

5. Case Study: Shuping Landslide

The Shuping landslide (Figure 6b) is a landslide that was reactivated when the Three Gorges Dam was built in June of 2003 and the artificial lake started filling. The area of the dam is formed, mainly, by sandy mudstone and muddy sandstone from the Triassic Badong formation (Wang et al., 2017). Because of this lithology, several landslides were triggered. Moreover, the Three Gorges Dam area is subject to long periods of rainfall, which is also another possible triggering factor of reactivation/formation of landslides (Huang et al., 2014).

In particular, the Shuping landslide has a sliding mass thickness between 30 and 70 m and a total sliding rock volume of 2.7×10^7 m³ (Figure 6c). Observations have shown that the landslide accelerates when the reservoir's level decreases, but the slide remains stable when the reservoir's level rises (Figure 6d) (Huang et al., 2014). Thus, from the field data, it can be seen that the Shuping landslide exhibits an opposite behavior from the Vaiont landslide (which accelerates when the lake level increases). This main difference in the behaviors of the two landslides can be traced to the permeability of the sliding mass, which is high in the case of Vaiont and low in the case of Shuping.

5.1. Geographical Location and Geological Framework

The Shuping landslide is located nearby the village of Xietanxiang, in Zigui county in eastern China. The slide lies on the southern crest of the valley, where the Yangtze River flows along. Downstream along the Yangtze River, at approximately 47 km, lies the Three Gorges Dam (Figure 6a) (Wang et al., 2017).

SEGUÍ ET AL. 15 of 24

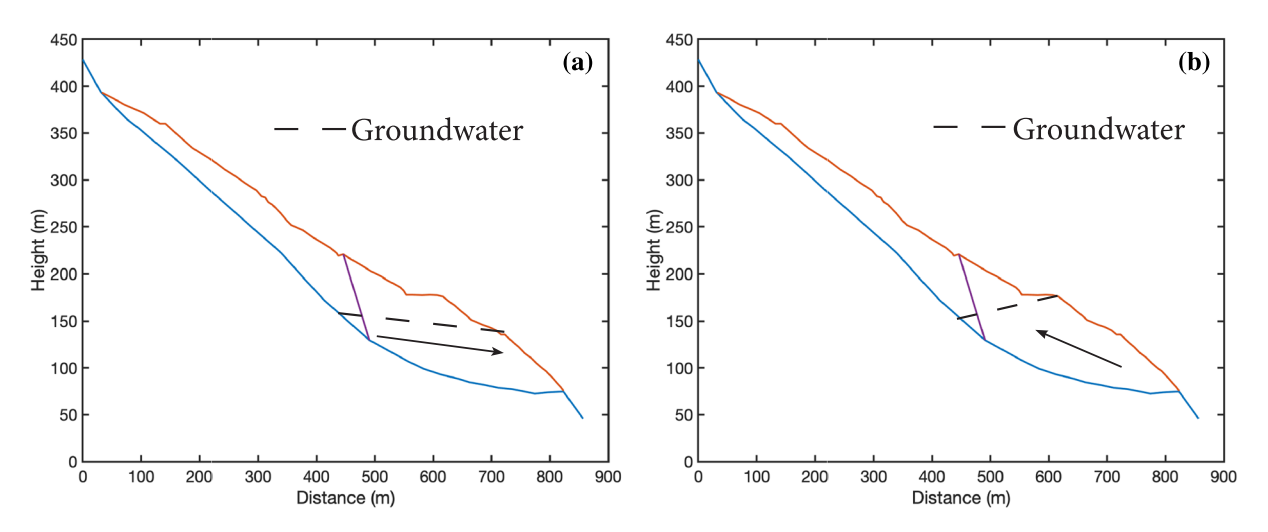


Figure 7. Schematic groundwater table (dashed line) scenarios, for a given cross section of the Shuping landslide: (a) when the reservoir level is lower than the piezometric level, allowing for positive slope of the groundwater table (similar to the Dupuit-Forchheimer profile of Figure 4c), and (b) when the reservoir level is higher than the piezometric level, allowing for negative slope of the groundwater table and thus of the seepage force. The black arrows show the direction of the seepage force for each case.

The landslide is geologically situated in the southern part of the Shazhenxi anticline, which is formed by mudstone, siltstone, and muddy limestone from the Triassic Badong formation. The layers of this formation, on the south side of the anticline, are dipping with an angle between 9 and 38° toward the direction of 120–173°. The highest part of the landslide is formed by gravel, and the bottom part of the landslide is formed by clay and silty clay. The mass is sliding over a thin layer (0.6–1 m) of brown breccia soil and silty clay, and the underlying material of the landslide is composed of siltstone mixed with mudstone (Yin et al., 2016).

The behavior of the landslide is shown in Figure 6d (Huang et al., 2014; Li, 2015). The groundwater of the landslide (reservoir level and piezometer level in Figure 6d) presents two different behaviors: (1) when the piezometer level is above the reservoir level (same direction of groundwater table slope as Vaiont) and 2) when the reservoir level is above the piezometer level (opposite slope as the Vaiont). Focusing now on the displacements that the sliding mass experience, Figure 6d shows that there is a delay between the high peaks of the water levels (reservoir and piezometer) and the acceleration of the landslide (displacement). This delay of the response of the landslide could indicate that the permeability of the sliding mass is low. We could also consider that the downdrawn of the reservoir level accelerates the sliding mass (i.e., destabilizes the landslide) (Huang et al., 2014).

5.2. Groundwater Analysis

To calculate the groundwater table for this case study, we apply the transient method (due to the delay between groundwater level peaks and the acceleration of the landslide, Figure 6d; Huang et al., 2014; Li, 2015) using the hydraulic head (Equation 6) and solving it analytically, with appropriate boundary conditions,

$$h(x = x_1) = U_1 \text{ and } h(x = x_2) = U_2$$
 (19)

obtaining

$$h(x, t) = \frac{(U_1 - U_2)\operatorname{erf}\left(\frac{\xi}{2}\right) + U_2\operatorname{erf}\left(\frac{\xi_1}{2}\right) - U_1\operatorname{erf}\left(\frac{\xi_2}{2}\right)}{\operatorname{erf}\left(\frac{\xi_1}{2}\right) - \operatorname{erf}\left(\frac{\xi_2}{2}\right)}$$
(20)

where $\xi_i = \frac{x_i}{2\sqrt{Dt}}$, and erf is the error function expressed as $\operatorname{erf}(z) = \frac{2}{\sqrt{\pi}} \int_0^z e^{-t^2} dt$, t is the time, h is the height of groundwater, U_1 is the height of the reservoir's level, U_2 is the height of groundwater at the

SEGUÍ ET AL. 16 of 24

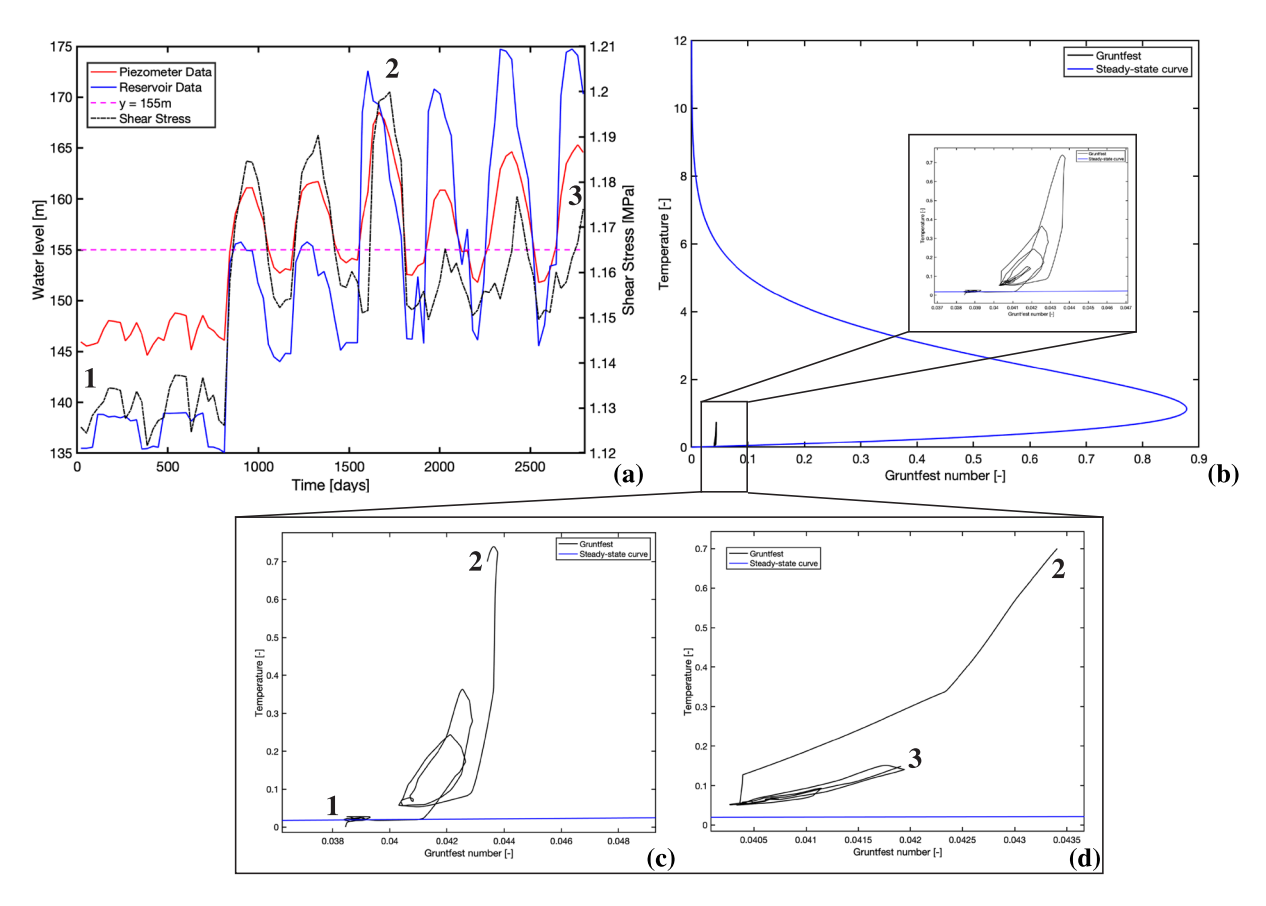


Figure 8. (a) Graph showing the reservoir level, the piezometer data, the value of the reservoir level when there is a zero-groundwater slope (no seepage force) as magenta dashed line, and the shear stress calculated for the Shuping slide. (b) Gruntfest number calculated versus temperature, with the steady-state curve. (c) Zoom of Figure 8b: Gruntfest number versus temperature for the first behavior of the landslide, Points 1 to 2 from Figure 8a. (d) Zoom of Figure 8b: Gruntfest number versus temperature for the second behavior of the landslide, Points 2 to 3 from Figure 8a.

fixed point in the back of the landslide, and x is the horizontal coordinate of a point between the two reference points of water level. Equation 20, thus, describes the hydraulic head evolution in time inside the sliding mass.

The boundary conditions chosen to calculate the hydraulic head (described in Equation 19) of the ground-water data are the reservoir's level and the piezometer data from the QZK3 piezometer (see Figure 6c for location; Wu et al. 2018). In Figures 7a and 7b, we represent the *two groundwater profiles* that the Shuping landslide experiences: (1) *positive seepage force* (pointing downward, when the piezometer level is above the reservoir's level) and (2) *negative seepage force* (pointing upward, when the reservoir's level is above the piezometer level), respectively. Note that the zero slope of the groundwater table is not presented in Figure 7.

5.3. Shear Stress Results

To calculate the shear stress (with the double-wedge method), we do not need to overestimate the basal shear stress value for this case study, as we use both the piezometer and reservoir's field data. Figure 8a presents the results of the basal shear stress calculated (at each reservoir and piezometer levels) as a function of time. In our results, the mean shear stress at the base of the landslide varies between 1.12 and 1.2 MPa, which are very similar values as the ones obtained for the Vaiont landslide.

As we have implemented the transient method to calculate the groundwater evolution, by applying a permeability value (Li, 2015), our shear stress results also show a time delay (between the high peaks of water and the high peaks of shear stress, Figure 8a). Figure 8a shows the evolution of shear stress, which compared to the groundwater data (reservoir and piezometer levels) has two different behaviors: (1) the shear stress is

SEGUÍ ET AL. 17 of 24



higher when the piezometer level is above the reservoir level (i.e., positive seepage force inside the sliding mass), and (2) the shear stress values are lower when the reservoir level is above the piezometer level (i.e., negative seepage force inside the sliding mass). Therefore, this could indicate that the landslide is decelerating by increasing the reservoir level (when the sliding mass has a negative seepage) force, and accelerating by decreasing reservoir level, when the seepage force is positive (i.e., seepage direction toward the reservoir level, downhill). A notable exception is the peak of stress at Point 2 of Figure 8a, which is admitted in the historically highest values of the piezometer and the reservoir levels, and after which an exchange of seepage direction is observed. The role of this point in the transient behavior of the slide will be discussed further in the following sections.

5.4. Transient Stability Analysis

In Table 1, we present the parameters of the clay material (inside the shear band) required to calculate the velocity of the landslide and the Gruntfest number. Some of these parameters have been taken from the Vaiont landslide (Veveakis et al., 2007) because of the absence of information for the Shuping landslide and because the shear bands are formed by similar clays. The rest of the parameters used for the Shuping landslide have been taken from Li (2015).

For the Shuping landslide, the mathematical system becomes unstable for a value of the Gruntfest number of 0.88 and a dimensionless maximum ratio of the temperature of 1.14 (Figure 8b). The critical value of the Gruntfest number, for the case of Shuping, is the same as for the Vaiont landslide. This is because the stability of the model is studied in a dimensionless form (Equation 16) with the Gruntfest number incorporating material properties and loading conditions that may vary in real case studies. It is therefore expected that this stability response is universal in the dimensionless space, for any material obeying the frictional law of Equation 10. Nonetheless, in order for the model to have forecasting capabilities, the Gruntfest number needs to be constrained with minimum uncertainty. In the following, we are performing an inverse analysis to estimate a value of the *Gr* from the displacement data for the case of Shuping, where detailed information of the material properties and loading is missing.

To calculate the velocity, we have chosen the Global Positioning System data provided by station ZG86 (Figure 6c for location and Figure 6d for the data). This is because we consider that (1) the location of this station represents an average displacement of the entire landslide and, (2) this station is the one that presents the largest displacements, which allows us to evaluate the stability for the worst-case scenario. Moreover, to fit the velocity calculated by our model with the data provided by the ZG86 station, we have used only one value of initial strain-rate (Figure 9). Comparing the two velocities (calculated and field data) in Figure 9, there are two main differences: (1) a change in the magnitude of some of the peaks and (2) a time lag between some peaks. The changes in magnitude and time lag indicate the difference between the model (which calculates an average velocity of the whole sliding mass) and the velocity of the field (which represents only the velocity of a single point of the sliding mass).

In the case of Vaiont, we know that the landslide collapses after the last filling of the reservoir; hence, the Gruntfest number reaches the steady-state curve causing the system to become unstable. However, in the Shuping landslide, the instability point (critical Gr) is uncertain because the landslide has not collapsed yet. Thus, we have calculated Gr with a value of N that matches as close as possible the field data (i.e., velocity), considering a rate sensitivity (parameter N) value within the range of values of clay materials reported in the literature. To constrain further this value (N), as well as the thermal sensitivity coefficient M in the Shuping case, and therefore offer predictive capabilities in the current approach, laboratory tests performed on the shear band's material would be required.

5.5. The Behavior of Shuping Landslide Explained Through Groundwater Regimes

Figures 6d and 8a show that the Shuping landslide admits two distinct behaviors over the ten years of its motion: (1) from Point 1 to Point 2 (Figure 9) where the seepage force tends downward, parallel to the slope of the landslide (Figure 7a). In this period, the piezometer's level was maintained above the reservoir's level, with both levels varying simultaneously and the landslide accelerating when the lake level decreased. (2) From Point 2 to Point 3 (Figure 9) the seepage is acting opposite to the slope of the landslide (Figure 7b). In this stage, the piezometer's level is maintained below the reservoir, consequently, inducing the inverse seepage. These two behaviors of the groundwater regime cause the landslide to accelerate when the reservoir level is decreased, in

SEGUÍ ET AL. 18 of 24

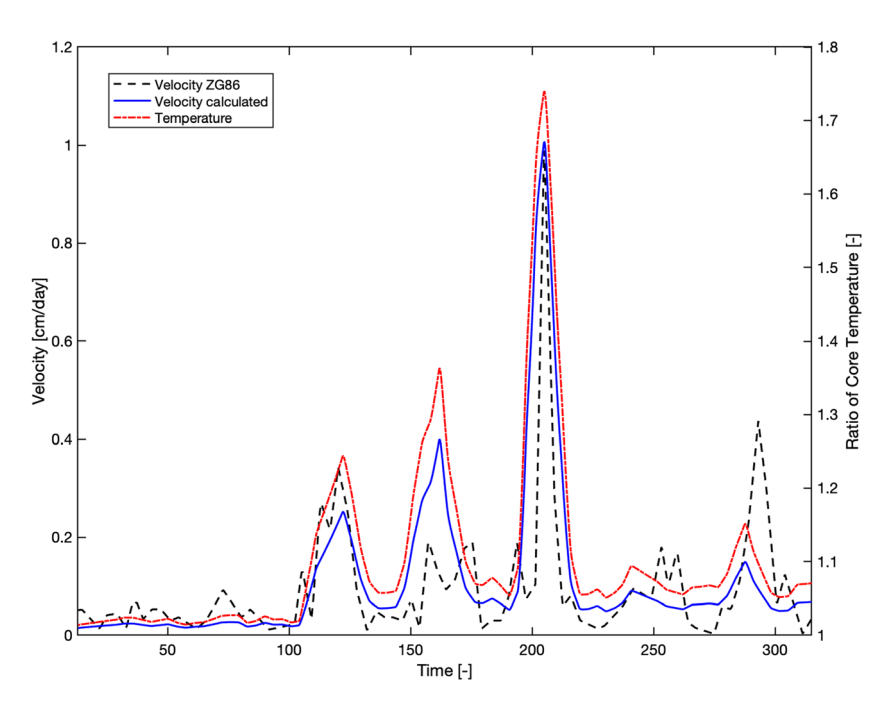


Figure 9. Velocity data from the field (calculated from the displacement obtained from Huang et al., 2014) shown as black dashed line. Velocity calculated from the model as blue. The red dashed/dotted line indicates the ratio of the real temperature with the reference temperature in the shear band.

accordance with other studies in the literature (Huang et al., 2014). Hence, it seems that keeping the reservoir on the second regime, thus maintaining the reservoir level above the piezometric level, would allow the landslide to be controlled easier, since increasing the lake level would decelerate the slope. However, since this is a transient regime, it is expected that when the reservoir head is consistently kept above the piezometric head within the landslide, groundwater would be flowing into the landslide, raising the hydraulic head and eventually negating the stabilizing effect. The timescale of this process depends on the hydraulic conductivity of the overburden mass and its volume. Therefore, any operation in this regime should consider these transient effects. (A/N: we thank the anonymous reviewer for highlighting this transient sequence).

6. Discussion and Conclusions

The cases of Vaiont and Shuping landslides were studied in this paper. For both cases, the implementation of a time-dependent shear stress in the thermal model presented in Veveakis et al. (2007) allowed us to reproduce the history of velocities for the Vaiont and Shuping slides. This model combines external and internal factors that drive the behavior of a landslide: the weakening of friction at the base of the slide (as the *internal factor*) and the pore pressure (i.e., the shear stress) evolution due to groundwater table variations (as the *external factor*). This combination of evolving external factors and internal response of the material allows for the identification of a coupled transient stability point for the landslides. Because this stability point is a combination of the effects of external loading and internal response, it allows extending the results of Veveakis et al. (2007) toward offering operational criteria for deep-seated creeping landslides. This could be achieved by measuring the shear-band material properties, which would allow identifying the critical loading conditions that would drive a landslide unstable (through its Gruntfest number) and operate below these critical conditions.

In this work, we have assumed a rigid (i.e., undeformable) block sliding over a visco-plastic shear band, with the material exhibiting *velocity hardening and thermal softening* as the two counteracting mechanisms. However, numerous additional mechanisms (such as slip weakening, volume change induced or thermal pressurization, weathering, and phase transformations) could also be triggered and reduce the shearing resistance of the basal material. Furthermore, a major assumption of the present work is that the landslides are creeping in a reactivation phase, allowing the material of the shear band to be considered at critical state,

SEGUÍ ET AL. 19 of 24



thereby deforming without any volume changes. This assumption eliminates the possibility of excess pore pressure generation inside the shear band due to volume changes, which has been shown in the literature (Garagash & Rudnicki, 2003; Iverson, 2005) to be a major mechanism that can destabilize Earth masses and landslides in particular (Alonso & Pinyol, 2010; Dykes & Bromhead, 2018a, 2018b; Vardoulakis, 2002b). It was adopted here because clay materials have experimentally shown to reach critical state after small amounts of accumulated shear strain, of the order of 1–2% (Tika & Hutchinson, 1999), and poses a strong limitation of the applicability of the present model to landslide events that are either a first-time event or not at critical state, or where the overburden is not rigid but deformable (Handwerger et al., 2016). Another limitation of the model is that the 1D nature of the shear band does not allow for two-dimensional effects like heat and mass advection to be admitted. These effects could prove of major importance in shear bands featuring high permeability that could further require extension of the current approach to more complicated, two-dimensional geometries.

Despite the strong limitations of the model for the basal material's response, the analysis included groundwater level variations (i.e., seasonal variations of the pore fluid pressure inside the landslide mass) which, in turn, feedback on the applied shear and normal stresses on the shear band's interface. The application of the model to the two case studies revealed that tracing the mechanical dissipation could determine the stability of the material, becoming unstable at the point where heat dissipation becomes significant enough to overcome the diffusive capabilities of the material and establish essentially adiabatic conditions. The inclusion of the groundwater variations offered the possibility of assessing this stability threshold in terms of reservoir level, precipitation, or groundwater level in general (Handwerger et al., 2016). Although the influence of the external factors (groundwater level variation) was shown not to be of primary importance to the evolution of the Vaiont landslide (the results we obtained were comparable to the results of Veveakis et al., 2007 with constant groundwater level), since the landslide seemed to be driven primarily by the internal response of the basal material, this is not the case for Shuping landslide. In the latter, the evolution of the groundwater level affects the response of the landslide strongly, as the seepage force is predominantly driving the loading stresses. In cases like this, where external and internal factors are simultaneously affecting the response of the slide, the present model can offer valuable information on the time-dependent stability threshold of the sliding mass.

Furthermore, the parameters used in reproducing the velocity history of both case studies (listed in Table 1) are falling within realistic range of values met in the literature. In the case of the Vaiont landslide, the values used for the parameters are comparable to the values used by Veveakis et al. (2007), with the notable exception of the reference strain-rate (which is orders of magnitude higher in this work). The reasons for this discrepancy are the differences in the boundary conditions imposed (in Veveakis et al., 2007 the system was solved as a Cauchy problem, without specifying boundary conditions) and that in the present study we are considering both a different time interval (we are inverting for 2 years of motion whereas Veveakis et al., 2007 only studied the last 6 months of the landslide) and a different shear stress evolution. In the present study, the shear stress is evolving with the groundwater level, ranging between 0.9 and 1.12 MPa, whereas Veveakis et al. (2007) considered a constant value of the shear stress of 1 MPa at an average groundwater level. It is therefore reasonable to say that, while in both cases (Vaiont and Shuping) we were able to determine a region of stability of the system, additional information on the properties of the shear band material is required to constrain further the values of the parameters and obtain a more accurate point of instability (especially for the currently active case of Shuping). This could be achieved, for example, by performing experimental shear tests on the shear band's material at various loading rates and temperatures.

In summary, we have shown with the analysis applied in this paper, that taking into account the energy balance inside the clayey gouge, the model allows to determine and calculate a stability point of the landslide. This method showcases that, even for different behaviors of landslides regarding the groundwater level, the approach could offer useful information to design operational protocols and procedures.

Appendix A: Limit Equilibrium Analysis for the Double Wedge Mechanism

The forces acting on Wedge 1 and Wedge 2 (Figure 2) are the weight and seepage, calculated considering a unit thickness. The weight W of each wedge is calculated as

SEGUÍ ET AL. 20 of 24

$$W = \gamma_{\text{sat}} A_{\text{sat}} + \gamma_{\text{dry}} A_{\text{dry}} \tag{A.1}$$

where $\gamma_{\rm dry}$ is the specific unit weight of the soil (a force defined as the density of the soil times the acceleration of gravity), $\gamma_{\rm dry}$ can also be calculated as the difference between $\gamma_{\rm sat}$ (the specific unit weight of saturated soil) and $\gamma_{\rm w}$ (the specific unit weight of water), $A_{\rm sat}$ is the area of saturated soil (beneath the groundwater table), and $A_{\rm dry}$ is the area of dry soil (above the groundwater table). The seepage force, S, acts as a positive force on each wedge (because this force follows the direction of the flux) and is calculated as

$$S = A_{\text{sat}} \gamma_{\text{w}} Dh = A_{\text{sat}} \gamma_{\text{w}} \sin\left(\frac{t+\beta}{2}\right)$$
(A.2)

where Dh is the difference of the hydraulic head (see Bear, 1972, chapter 8, for an in-depth discussion on the geometric representation of the hydraulic head difference in an unconfined aquifer).

Applying the Earth pressure theory of Rankine (see chapter 11 of Craig, 2004), we can calculate the active and the passive forces of the landslide. The active force (i.e., the force acting on Wedge 2 from Wedge 1) is

$$E_{12} = \left(0.5 \,\gamma_{\text{sat}} \,H_{\text{sat}}^2 \,k_{\text{a}} - 2 \,c \,H_{\text{sat}} \,\sqrt{k_{\text{a}}}\right) + \left(0.5 \,\gamma_{\text{dry}} \,H_{\text{dry}}^2 \,k_{\text{a}} - 2 \,c \,H_{\text{dry}} \,\sqrt{k_{\text{a}}}\right) \tag{A.3}$$

where $H_{\rm sat}$ and $H_{\rm dry}$ are the normalized heights of saturated and dry soil, respectively, at the interface line between the two wedges, c is the cohesion, and $k_{\rm a}$ is the active lateral Earth pressure coefficient calculated as follows:

$$k_{\rm a} = \frac{\sin^2(\alpha_1 + \phi)}{\sin^2\alpha_1\sin(\alpha_1 - \delta_2)\left[1 + \sqrt{\frac{\sin(\phi + \delta_2)\sin(\phi - \beta_2)}{\sin(\alpha_1 - \delta_2)\sin(\alpha_1 + \beta_2)}}\right]} \tag{A.4}$$

with α_1 being the angle of the interface line (which divides the two blocks) with the horizontal, ϕ is the friction angle, δ_2 is set at 2/3 of the friction angle (Craig, 2004), and β_2 is the angle of the topography of the Wedge 2 against the horizontal.

The passive Earth force, E_{21} (i.e., the force acting on Wedge 1 from Wedge 2), is calculated as

$$E_{21} = \left(0.5 \,\gamma_{\text{sat}} \,H_{\text{sat}}^2 \,k_{\text{p}} - 2 \,c \,H_{\text{sat}} \,\sqrt{k_{\text{p}}}\right) + \left(0.5 \,\gamma_{\text{dry}} \,H_{\text{dry}}^2 \,k_{\text{p}} - 2 \,c \,H_{\text{dry}} \,\sqrt{k_{\text{p}}}\right) \tag{A.5}$$

where k_p is the passive lateral Earth pressure coefficient, calculated as follows:

$$k_{p} = \frac{\sin^{2}(\alpha_{2} - \phi)}{\sin^{2}\alpha_{2}\sin(\alpha_{2} + \delta_{1})\left[1 - \sqrt{\frac{\sin(\phi + \delta_{1})\sin(\phi + \beta_{1})}{\sin(\alpha_{2} + \delta_{1})\sin(\alpha_{2} + \beta_{1})}}\right]}$$
(A.6)

In this expression A.6, α_2 is calculated as $\alpha_2 = \pi - \alpha_1$, δ_1 is 1/3 times the friction angle (Craig, 2004), and β_1 is the angle of the topography of the Wedge 1 with the horizontal.

Thus, the equilibrium of horizontal forces acting at the center of mass of Wedge 1 gives:

$$T + E_{21H} - S\cos(\beta_2 - \alpha_2) + N\sin(\varphi') - W\cos(\beta_2) = 0$$
 (A.7)

where *N* is the normal force acting on both wedges, *T* is the shear force acting at the bottom of the wedge (as negative on both wedges), and φ' is the friction angle of the soil.

Correspondingly, horizontal force equilibrium at the center of mass of the Wedge 2 is

$$T - E_{12H} - S\cos(\beta_1 - \alpha_1) + N\sin(\varphi') - W\cos(\beta_1) = 0$$
(A.8)

where β_1 is the slope of the sliding surface of the Wedge 1 with the horizontal.

SEGUÍ ET AL. 21 of 24

The vertical equilibrium forces acting on Wedge 1 (Equation A.9) and on Wedge 2 (Equation A.10) are

$$N\cos(\phi') - W\sin(\beta_2) + S\sin(\beta_2 - \alpha_2) + E_{21V} = 0 \tag{A.9}$$

$$N\cos(\varphi') - W\sin(\beta_1) + S\sin(\beta_1 - \alpha_1) - E_{12V} = 0$$
 (A.10)

Hence, we calculate the normal (N) and shear (S) forces (as a system of equations) for Wedge 1 with Equations A.7 and A.9, and for Wedge 2 with Equations A.8 and A.10. The forces calculated by Equations A.7–A.10 are referred to as the center of mass of each wedge. Thus, applying the results of the forces to the conceptual Model B, the shear stress forces calculated are admitted in the shear band (i.e., the base of the infinite rigid-elastic block). By then dividing S by the length, L, (assuming unit-length in the third direction) of the sliding surface, we calculate the mean basal shear stress force of the landslide (Muller, 1968) to populate the average values of Equation 8. In addition, the values of $H^{(1)}$ and $H^{(2)}$ from Equation 8 are the total height of each wedge transformed into an infinite block (Figure 1b). Each wedge height is calculated as follows:

$$H^{(1)} = H_{\text{sat}}^{(1)} + H_{\text{dry}}^{(1)} \tag{A.11}$$

$$H^{(2)} = H_{\text{sat}}^{(2)} + H_{\text{dry}}^{(2)} \tag{A.12}$$

where the indices (1) and (2) indicate the wedge, $H_{\rm sat}$ is the height of the saturated material, and $H_{\rm dry}$ is the height of the dry material. To obtain the dry and saturated heights of each wedge, we have taken the areas calculated (saturated and dry) and divide them by a large value of horizontal distance (for example, 100 m) to transform the real shape of the landslide (Figure 1a) into an infinite block (Figure 1b).

Acknowledgments References

Most of the concepts presented in this

friendship of E. Veveakis with late I.

ideas was in place since early 2008

when E.V. and I.V. were working

together on the Vaiont landslide.

Vardoulakis. An early version of these

Because of his untimely passing in mid-

2009, these ideas never materialized in

a concrete scientific publication. The

fruit of these ideas and is therefore

Vardoulakis, for his guidance and

present work is seen to be the ripened

full-heartedly dedicated to late Ioannis

inspirational ideas. The authors would like to acknowledge the contribution of

improving the manuscript substantially

during the review process. Support by

the NSF CMMI-2006150 project is also

obtained with GPS stations are openly

the Editor, Noah Finnegan, and the

three anonymous reviewers in

acknowledged. The data of the

groundwater table obtained with

available at https://eartharxiv.org/

ukbr5/

piezometers, and displacements

work are the result of close

collaboration, mentorship, and

Alevizos, S., Poulet, T., & Veveakis, E. (2014). Thermo-poro-mechanics of chemically active faults. 1: Theory and steady-state considerations. *Journal of Geophysical Research: Solid Earth*, 119, 4558–4582. https://doi.org/10.1002/2013JB010070

Alonso, E., (1989a). Análisis de la estabilidad de taludes. Casos simples. En Corominas, J. (editor), "Estabilidad de Taludes y Laderas Naturales", Monografía n° 3, Sociedad Española de Geomorfología, pp. 97–118.

Alonso, E., (1989b). Métodos generales de equilibrio límite. En Corominas, J. (editor), "Estabilidad de Taludes y Laderas Naturales", Monografía nº 3, Sociedad Española de Geomorfología, pp. 119–166.

Alonso, E. E., & Pinyol, N. M. (2010). Criteria for rapid sliding I. A review of Vaiont case, Engineering Geology, 114(3-4), 198–210. https://doi.

org/10.1016/j.enggeo.2010.04.018

Alonso, E. E., Zervos, A., & Pinyol, N. M. (2016). Thermo-poro-mechanical analysis of landslides: From creeping behaviour to catastrophic failure. *Géotechnique*, 66(3), 202–219. https://doi.org/10.1680/jgeot.15.LM.006

Anderson, D. L. (1980). An earthquake induced heat mechanism to explain the loss of strength of large rock and earth slides. In *Proceedings* of the International Conference on Engineering for Protection from Natural Disasters, (pp. 569–580). New York: John Wiley.

Bagnold, R. A. (1954). Experiments on a gravity free dispersion of large solid spheres in a Newtonian fluid under shear. *Proceedings of the Royal Society of London, Series A*, 225, 49–63.

Bear, J. (1972). Dynamics of Fluids in Porous Media. (764 p.) New York: American Elsevier Publishing Company. ISBN-13: 978-0-486-65675-5

Cecinato, F., Zervos, A. (2012). Influence of thermomechanics in the catastrophic collapse of planar landslides. *Canadian Geotechnical Journal.*, 49, No. 2, 207–225.

Cecinato, F., Zervos, A., & Veveakis, E. (2011). A thermo-mechanical model for the catastrophic collapse of large landslides. *International Journal for Numerical and Analytical Methods in Geomechanics*, 35(14), 1507–1535. https://doi.org/10.1002/nag.963

Chan, T. F. C., & Keller, H. B. (1991). Arc-length continuation and multi-grid techniques for nonlinear elliptic eigenvalue problems. SIAM Journal on Scientific and Statistical Computing, 3(2), 173–194.

Craig, R. F. (2004). Craig's Soil Mechanics. (7th ed.). Taylor & Francis. ISBN: 9780415327039.

Dykes, A. P., & Bromhead, E. N. (2018a). The Vaiont landslide: Re-assessment of the evidence leads to rejection of the consensus. Landslides, 15(9), 1815–1832. https://doi.org/10.1007/s10346-018-0996-y

Dykes, A. P., & Bromhead, E. N. (2018b). New, simplified and improved interpretation of the Vaiont landslide mechanics. *Landslides*, 15(10), 2001–2015. https://doi.org/10.1007/s10346-018-0998-9

Ferri, F., Di Toro, G., Hirose, T., Han, R., Noda, H., Shimamoto, T., et al. (2011). Low- to high-velocity frictional properties of the clay-rich gouges from the slipping zone of the 1963 Vaiont slide, northern Italy. *Journal of Geophysical Research*, 116, B09208. https://doi.org/10.1029/2011JB008927

Garagash, D. I., & Rudnicki, J. W. (2003). Shear heating of a fluid-saturated slip-weakening dilatant fault zone 1. Limiting regimes. *Journal of Geophysical Research*, 108(B2), 2121. https://doi.org/10.1029/2001JB001653

Goren, L., & Aharonov, E. (2007). Long runout landslides: The role of frictional heating and hydraulic diffusivity. Geophysical Research Letters, 34, L07301. https://doi.org/10.1029/2006GL028895

Goren, L., & Aharonov, E. (2009). On the stability of landslides: A thermo-poro-elastic approach. *Earth and Planetary Science Letters*, 277(3-4), 365–372.

Goren, L., Aharonov, E., & Anders, M. H. (2010). The long runout of the Heart Mountain landslide: Heating, pressurization, and carbonate decomposition. *Journal of Geophysical Research*, 115, B10210. https://doi.org/10.1029/2009JB007113

SEGUÍ ET AL. 22 of 24



- Gruntfest, I. J. (1963). Thermal feedback in liquid flow: Plane shear at constant stress. *Transactions. Society of Rheology*, 7(1), 195–207. https://doi.org/10.1122/1.548954
- Handwerger, A. L., Rempel, A. W., Skarbek, R. M., Roering, J. J., & Hilley, G. E. (2016). Rate-weakening friction characterizes both slow sliding and catastrophic failure of landslides. *Proceedings of the National Academy of Sciences*, 113(37), 10281–10286. https://doi.org/ 10.1073/pnas.1607009113
- Helmstetter, A., Sornette, D., Grasso, J. R., Andersen, J. V., Gluzman, S., & Pisarenko, P. (2004). Slider block friction model for landslides: Application to Vaiont and La Clapière landslides. *Journal of Geophysical Research*, 109, B02409. https://doi.org/10.1029/2002JB002160
- Hendron, A. J., & Patton, F. D. (1985). The Vaiont Slide: A Geotechnical Analysis Based on New Geologic Observations of the Failure Surface, Volume 1: Main Text. Washington, DC: Department of the Army US Corps of Engineers.
- Huang, H., Yi, W., Lu, S., Yi, Q., & Zhang, G. (2014). Use of monitoring data to interpret active landslide movements and hydrological triggers in Three Gorges reservoir. Journal of Performance of Constructed Facilities, 30(1).
- Hueckel, T., & Baldi, G. (1990). Thermoplastic behavior of saturated clays: An experimental constitutive study. *Journal of Geotechnical Engineering*, 116(12), 1778–1796. https://doi.org/10.1061/(ASCE)0733-9410(1990)116:12(1778)
- Iverson, R. M. (2005). Regulation of landslide motion by dilatancy and pore pressure feedback. *Journal of Geophysical Research*, 110, F02015. https://doi.org/10.1029/2004JF000268
- Kilburn, R. J. C., & Petley, D. M. (2003). Forecasting giant, catastrophic slope collapse: Lessons from Vajont. Northern Italy, Geomorphology, 54(1-2), 21–32. https://doi.org/10.1016/S0169-555X(03)00052-7
- Lachenbruch, A. H. (1980). Frictional heating, fluid pressure and the resistance to fault motion. *Journal of Geophysical Research*, 85(B11), 6097–6112. https://doi.org/10.1029/JB085iB11p06097
- Leinenkugel, H.-J. (1976). Deformations und festigkeitverhalten bindiger erdstoffe: Experimental ergebnisse und ihre physikalische deutung", doctoral Dissertation. Karlsruhe, Germany: Univ. Karlsruhe.
- Li, Y. (2015). Mechanism of landslides around China's Three Gorges dam (Master thesis). University of Alberta, Department of Civil and Environmental Engineering.
- Ma, J., Tang, H., Liu, X., Wen, T., Zhang, J., Tan, Q., & Fan, Z. (2017). Probabilistic forecasting of landslide displacement accounting for epistemic uncertainty: A case study in the Three Gorges reservoir area. China. Landslides, 15(6), 1145–1153. https://doi.org/10.1007/ s10346-017-0941-5
- Mase, C. W., & Smith, L. (1984). Pore-fluid pressures and frictional heating on a fault surface. PAGEOPH, 122(2-4), 583-607. https://doi.org/10.1007/BF00874618
- Muller, L. (1964). The rock slide in the Vaiont valley. Felsmech. Ingenoirgeol, 2, 148-212.
- Muller, L. (1968). New considerations on the Vaiont slide. Felsmech. Ingenoirgeol, 6, 1-91.
- Picard, J. (1994). Ecrouisage thermique des argiles saturées: Application au stockage des déchets radioactifs. Thèse de Doctorat. Paris, France: Ecole Nationale des Ponts et Chaussées.
- Pinyol, N. M., & Alonso, E. E. (2010). Criteria for rapid sliding II. Thermo-hydro-mechanical and scale effects in Vaiont case, Engineering Geology, 114, 211–227.
- Poulet, T., Veveakis, E., Regenauer-Lieb, K., & Yuen, D. A. (2014). Thermo-poro-mechanics of chemically active creeping faults. 3: The role of serpentinite in episodic tremor and slip sequences, and transition to chaos. *Journal of Geophysical Research: Solid Earth*, 119, 4606–4625. https://doi.org/10.1002/2014JB011004
- Rice, J. (2006). Heating and weakening of faults during earthquake slip. *Journal of Geophysical Research*, 111, B05311. https://doi.org/10.1029/200JB004006
- Saito, M. (1965). Forecasting the time of occurrence of slope failure. Proceeding of the 6th International Conference on Soil Mechanics and Foundation Engineering, Montreal (Vol. 2, pp. 537–541).
- Saito, M. (1969). Forecasting time of slope failure by tertiary creep. Proceedings of the 7th International Conference on Soil Mechanics and Foundation Engineering, Mexico City (Vol. 2, pp. 677–683).
- Semenza, E., & Melidoro, E. (Eds.), (1992). Proceedings of the meeting on the 1963 Vaiont landslide, IAEG Italian Section and Dip Sc Geologiche e Paleontologiche University of Ferrara 1. (pp. 1–218).
- Song, K., Yan, E., Zhang, G., & Yi, Q. (2014). Back analysis of hydraulic properties for a landslide in the Three Gorges Area. Advances in Transportation Geotechnics and Materials for Sustainable Infrastructure. (pp. 89–97).
- Sornette, D., Helmstetter, A., Andersen, J. V., Gluzman, S., Grasso, J. R., & Pisarenko, V. (2004). Towards landslide predictions: Two case studies. *Physica A*, 338(3–4), 605–632. https://doi.org/10.1016/j.physa.2004.02.065
- Terzaghi, K. (1950). Mechanism of landslides. In *Application of Geology to Engineering Practice*, (pp. 83–123). Harvard University, Cambridge, MA: Geological Society of America. https://doi.org/10.1130/Berkey.1950.83
- Tika, T. E., & Hutchinson, J. N. (1999). Ring shear tests on soil from the Vaiont landslide slip surface. *Géotechnique*, 49(1), 59–74. https://doi.org/10.1680/geot.1999.49.1.59
- Vardoulakis, I. (2002a). Dynamic thermo-poro-mechanical analysis of catastrophic landslides. Géotechnique, 52(3), 157–171. https://doi.org/10.1680/geot.2002.52.3.157
- Vardoulakis, I. (2002b). Steady shear and thermal run-away in clayey gouges, Int. *Journal of Solids and Structures*, 39(13-14), 3831–3844. https://doi.org/10.1016/S0020-7683(02)00179-8
- Veveakis, E., Alevizos, S., & Vardoulakis, I. (2010). Chemical reaction capping of thermal instabilities during shear of frictional faults. Journal of the Mechanics and Physics of Solids, 58(9), 1175–1194. https://doi.org/10.1016/j.jmps.2010.06.010
- Veveakis, E., Poulet, T., & Alevizos, S. (2014). Thermo-poro-mechanics of chemically active faults. 2: Transient considerations. *Journal of Geophysical Research: Solid Earth*, 119, 4583–4605. https://doi.org/10.1002/2013JB010071
- Veveakis, E., & Regenauer-Lieb, K. (2015). Cnoidal waves in solids. Journal of the Mechanics and Physics of Solids, 78, 231–248. https://doi.org/10.1016/j.jmps.2015.02.010
- Veveakis, E., Vardoulakis, I., & Di Toro, T. (2007). Thermoporomechanics of creeping landslides: The 1963 Vaiont slide, northern Italy. Journal of Geophysical Research, 112(F3), F03026. https://doi.org/10.1029/2006JF000702
- $Voight, B.\ (1988).\ A\ method\ for\ prediction\ of\ volcanic\ eruptions.\ \textit{Nature,}\ 332 (6160),\ 125-130.\ https://doi.org/10.1038/332125a0.\ https://d$
- Voight, B., & Faust, C. (1982). Frictional heat and strength loss in some rapid landslides. Géotechnique, 32(1), 43–54. https://doi.org/ 10.1680/geot.1982.32.1.43
- Wang, D. J., Tang, H.-M., Zhang, Y.-H., Li, C.-D., & Huang, L. (2017). An improved approach for evaluating the time-dependent stability of colluvial landslides during intense rainfall. *Environment and Earth Science*, 76(8), 321. https://doi.org/10.1007/s12665-017-6639-0

SEGUÍ ET AL. 23 of 24



- Wu, Q., Tang, H., Ma, X., Wu, Y., Hu, X., Wang, L., et al. (2018). Identification of movement characteristics and casual factors of the Shuping landslide based on monitored displacements. *Bulletin of Engineering Geology and the Environment*, 78(3), 2093–2106. https://doi.org/10.1007/s10064-018-1237-2
- Yin, Y., Huang, B., Wang, W., Wei, Y., Ma, X., & Ma, F. (2016). Reservoir-induced landslides and risk control in Three Gorges project on Yangtze River, China. *Journal of Rock Mechanics and Geotechnical Engineering*, 8(5), 577–595. https://doi.org/10.1016/j.irmge.2016.08.001
- Yu, Z., Xu, G., & Li, W. (2017). Deformation investigation and stability analysis of large-scale controlled reservoir landslides in Badong County, Three Gorges reservoir. Revista de la Facultad de Ingenieria U.C.V, 32(16), 655–668.
- Zhao, Y., Li, Y., Zhang, L., & Wang, Q. (2016). Groundwater level prediction of landslide based on classification and regression tree. *Geodesy and Geodynamics*, X(X), 1–8.

SEGUÍ ET AL. 24 of 24